Beam Instrumentation and Diagnostics

Peter Forck
GSI Helmholtz-Zentrum für Schwerionenforschung, Darmstadt, Germany

Abstract

The determination of beam parameters is essential for the operation and development of any accelerator facility. The working principle of frequently used beam instruments for electron and proton beams is discussed. The article comprises of the beam instrumentation for beam current determination, the usage of beam position monitors for bunched beams, methods for transverse profile and emittance diagnostics, bunch shape measurement and the usage of beam loss monitors.

Keywords

Beam instrumentation; current transformer; position and profile monitor; emittance measurement; beam loss monitor.

1 Demands for beam diagnostics

Beam diagnostics is an essential constituent of any accelerator as it is the sensory organ showing the properties and the behaviour of the beam. It deals with the real beam including all possible imperfections of a real technical installation. There is a vast range of applications for the diagnostics resulting in quite different demands for the beam instruments and the related display of the measurement results:

– Reliable, quick measurements to determine the basic parameters of a machine setting are used as a fast check of the general functionality of the accelerator. The readings from the instrumentation give a single number or simple plots. These devices should be non-destructive for the beam, yielding online information. A prominent example is a current measurement by a current transformer, as discussed in Section 2.

– Instruments are installed for a daily check of performance and stability or the control of necessary parameter changes in the accelerator setting. They are also used for solving simpler machine problems in case of any device malfunction. An example is the transverse profile determination, in most cases performed by a destructive device, as discussed in Section 4.

– Complex instrumentation for the commissioning of a new accelerator component, for the development of higher performance and for solving more serious problems in case of a malfunction must be available. The devices can be more complex to use and might be destructive for the beam. The determination of the beam emittance is an example as discussed in Section 5.

– An additional application is the active control of device settings after the detection of the beam's properties where the beam instrumentation serves as the sensor. This is generally called feedback of a given parameter to yield an improved beam delivery. An example is the determination of the beam position inside a synchrotron and the correction of the orbit to its nominal value.

General articles and books on beam instrumentation and its usage for beam diagnostics are Refs. [1–7].

The outline of this contribution is oriented on the beam quantities. Section 2 describes the measurement of beam current by current transformers in a non-interfering manner and Faraday Cup as an invasive device. Section 3 covers the frequent usage of beam position monitors which delivers the transverse centre-of-mass of a bunched beam. In nearly all facilities these instruments are used for the daily beam alignment as well as the monitor for advanced diagnostics. Section 4 describes several methods for transverse profile measurements. There are methods which can be operated for all beams, but also quite

different methods are used for electrons (which are in most cases relativistic) and protons (which require a large facility to reach relativistic velocities). Some of these methods are destructive for the beam and cannot, therefore, be applied at a synchrotron to monitor the beam properties of the circulating beam. Section 5 deals with the determination of transverse emittance in transfer lines, where the statistical description of the ensemble of beam particles is relevant. Section 6 deals with the determination of longitudinal parameters, with the focus on bunch shape determination at circular and linear light sources. In the last section, monitors detecting the lost beam are discussed. Generally, the basic functionality of the beam instrumentation is discussed, including some examples of related measurements; more details and applications can be found in the references.

2 Measurement of beam current

The total electrical current is one of the most important parameters for the operation of a particle accelerator. In the daily operation, a first check concerns the current in almost all accelerator laboratories; in most cases, it is measured with a beam current transformer. Several types of current transformers are available to determine the current at electron and proton LINACs and synchrotrons, even for short pulses, such as for the transfer between synchrotrons, as well as for coasting beams, such as for storage rings. These devices are commercially available [8], even though quite different types are used, a general overview of the current measurement device is presented in [9]. Current transformers are generally non-intercepting devices. Their principle is the detection of the magnetic field carried by the beam. For currents below about 1 μA, transformers cannot be used owing to noise limitations.

From the first days of accelerators, Faraday cups were used. The cup gives a direct measurement of the particle beam's charge because the particles are stopped in the cup. For high current, this destructive method can not be applied, because the total energy carried by the beam can destroy the intercepting material. For higher energetic particles with energies above some 100 MeV/u for ions, the penetration depth reaches more than several cm, and Faraday cups are not useful any more.

2.1 Current transformer for pulsed beams

In an accelerator the current is formed by N_{part} particles of charge state q per unit of time t or unit of length l and velocity $\beta = v/c$. The electrical current passing a given location is

$$I_{beam} = \frac{qeN_{part}}{t} = \frac{qeN_{part}}{l} \cdot \beta c \tag{1}$$

with e being the elementary charge. The magnetic field B of a current can be calculated according to the Biot-Savart law

$$\mathrm{d}\vec{B}(\vec{r}) = \mu_0 I_{beam} \cdot \frac{\mathrm{d}\vec{l} \times \vec{r}}{4\pi r^3} \tag{2}$$

with $\mu_0 = 4\pi \cdot 10^{-7}$ Vs/Am is the permeability of the vacuum, $\vec{dl}$ the length in direction of the beam and $\vec{r}$ the distance between the centre of the beam and the location of the field determination. Due to the cylindrical symmetry outside of the beam only the azimuthal component has to be considered along the unitary vector $\vec{e}_\varphi$ as shown in Fig. 1

$$\vec{B} = \mu_0 \frac{I_{beam}}{2\pi r} \cdot \vec{e}_\varphi. \tag{3}$$

For a beam current of 1 μA and a distance of 10 cm the magnetic field has a value of only 2 pT. To put this into perspective, the Earth magnetic field has a value of about 50 μT.

The beam current can be determined by monitoring the accompanying magnetic field with a current transformer schematically shown in Fig. 2. The beam passes through a highly permeable torus as the 'primary winding'. An insulated wire wound around the torus with N turns serve as the 'secondary
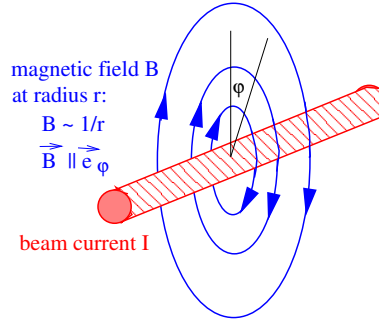
Fig. 1: The magnetic field of a current.
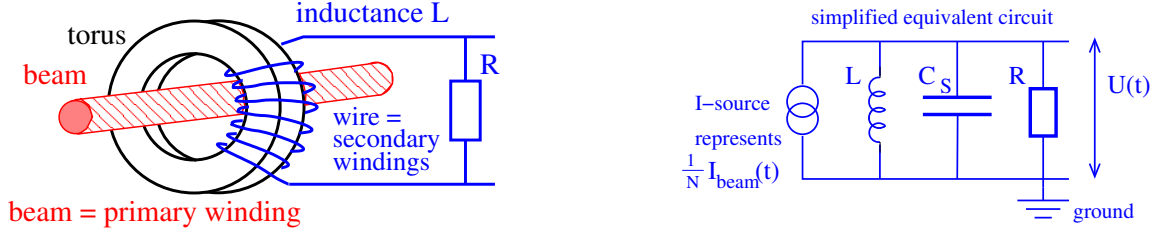
Fig. 2: Left: Scheme of a current transformer built as a ring-core (torus) around the beam. Right: Simplified equivalent circuit.

winding' of the transformer with the inductance L. The inductance L for a torus material of length l in beam direction, inner radius r_i and outer radius r_o having a relative permeability μ_r and N windings is given by

$$L = \frac{\mu_0 \mu_r}{2\pi} \cdot l N^2 \cdot \ln \frac{r_o}{r_i}. \tag{4}$$

The value of the induction can be chosen by the core size (as given by r_i and r_o) and the number of windings N. A further reason for the torus is to guide the field-lines, so only the azimuthal component is measured and the signal strength is nearly independent of the beam position inside the vacuum pipe.

Generally, for an ideal current transformer loaded with a low value of ohmic resistance R the ratio between the primary current I_{prim} conducted in N_{prim} windings and the secondary current I_{sec} conducted in N_{sec} is given by

$$I_{sec} = \frac{N_{prim}}{N_{sec}} \cdot I_{prim} \implies I_{sec} = \frac{1}{N} \cdot I_{prim} \quad \text{due to } N_{prim} = 1 \tag{5}$$

$N_{prim} = 1$ is one due to the single pass of the beam through the torus. N_{sec} is the winding number on the secondary side and for simplicity it is called N further-on.

For most practical cases a measurement of a voltage U is preferred, therefore the resistance R is introduced leading to

$$U = R \cdot I_{sec} = \frac{R}{N} \cdot I_{beam} \ . \tag{6}$$

The ratio between the usable signal voltage U and the beam current I_{beam} is called sensitivity S (or transfer impedance, for a more stringent discussion see Section 3.1)

$$U = S \cdot I_{beam} \quad . \tag{7}$$

The properties of a transformer can be influenced by different external electrical elements to match the response to a given time structure of the beam. We first consider the characteristics of a so-called passive transformer or **F**ast **C**urrent **T**ransformer **FCT**, where the voltage at a 50 Ω resistor is recorded.
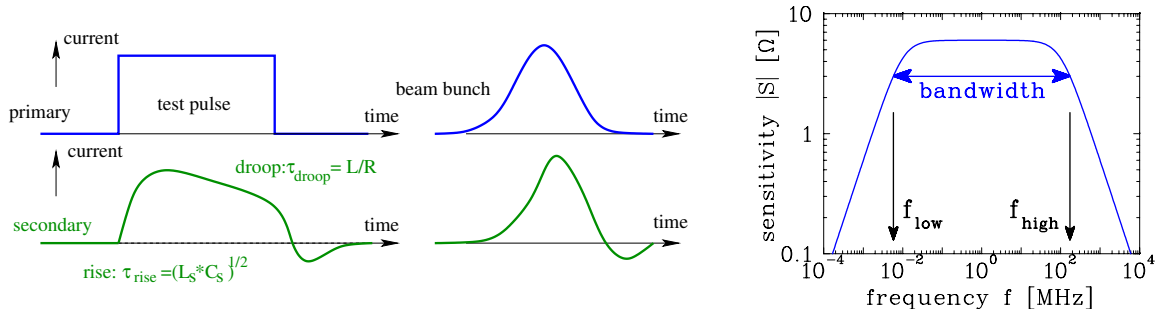
Fig. 3: Left: The response of a transformer to a rectangular pulse and a more realistic beam pulse. Right: The corresponding frequency domain plot for the sensitivity as a function of frequency.

The equivalent circuit of the secondary transformer side is depicted in Fig. 2 on the right side. The beam current is modelled by a current source with a reduction given by the number of windings N according to Eq. 5. One has to take also some stray capacitance C_S into account, which are caused by the capacitance between the windings, the windings and the torus and along the shielded cable to the resistor R. Generally, the voltage $U(t)$ of the parallel shunt of the three elements is measured. Depending on the choice of elements the response is influenced as discussed in the general textbooks on beam diagnostics the review article on transformers [2–4, 7, 9]; here we state only the results.

For the following discussion, we are interested in the time response of the measurement device to a given beam pulse. Therefore, one uses frequently the rise time constant τ_{rise} and the droop time constant τ_{droop} as depicted in Fig. 3: If the excitation is given by a step function, the signal amplitude A increases as $A \propto (1 - e^{-t/\tau_{rise}})$ and τ_{rise} corresponds to the time for an increase by $e^{-1} = 37$ %. It is linked to the upper cut-off frequency by

$$\tau_{rise} = \frac{1}{\omega_{high}} = \frac{1}{2\pi f_{high}} \quad . \tag{8}$$

Correspondingly, the droop time constant is linked to the lower cut-off frequency as

$$\tau_{droop} = \frac{1}{2\pi f_{low}} \quad . \tag{9}$$

Both equations have a general meaning and will be used to transfer quantities like bandwidth, as given in the frequency domain, into the corresponding description in the time domain

For the passive current transformer as described by the equivalent circuit of Fig. 2 the rise and droop time constant are given by

$$\tau_{rise} = RC_S \quad \text{and} \quad \tau_{droop} = \frac{L}{R} \quad . \tag{10}$$

A more realistic schematic diagram of the passive transformer is shown in Fig. 4. The main difference is the additional loss resistivity in the cables, which is represented by a serial resistor R_L. Additionally, there is a stray inductance between the windings, which is best modelled by a serial insertion of an inductance L_S. With these two modifications the rise and droop times are modified to yield

$$\tau_{rise} = \sqrt{L_S C_S} \quad \text{and} \quad \tau_{droop} = \frac{L}{R + R_L} \quad . \tag{11}$$

The specifications of the GSI device are listed in Table 1. Careful matching is necessary between the torus and the 50 Ω resistor R, where the voltage drop is measured.
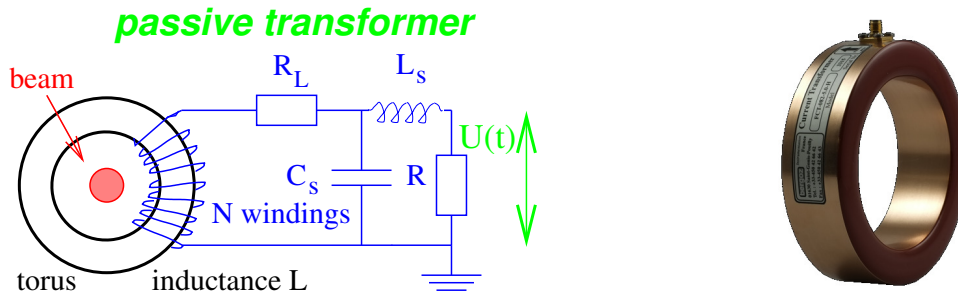
Fig. 4: Left: Equivalent circuits of a passive beam transformer. Right: Photo of a commercially available passive transformer [8].

Table 1: Basic specification of the GSI passive transformer [11].

Parameter	Value
Torus radii	$r_i = 70$ mm, $r_o = 90$ mm
Torus thickness l	16 mm
Torus material	Vitrovac 6025: $(CoFe)_{70\%}(MoSiB)_{30\%}$
Torus permeability μ_r	$\mu_r \simeq 10^5$ for $f < 100$ kHz, $\mu_r \propto 1/f$ above
Number of windings N	10
Sensitivity S	4 V/A at $R = 50\ \Omega$ (10^4 V/A with amplifier)
Current resolution I_{min}	40 μA_{rms} for full bandwidth
Droop time constant $\tau_{droop} = L/R$	0.2 ms, corresponding to 5% per 10 μs pulse length
Rise time constant $\tau_{rise} = \sqrt{L_S C_S}$	1 ns
Bandwidth	$f_{low} = 0.75$ kHz to $f_{high} = 660$ MHz
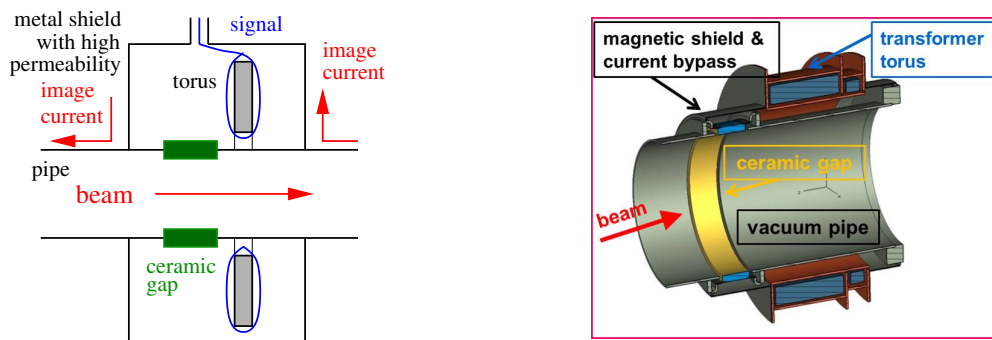
Fig. 5: Left: The general scheme beam pipe intersected by a ceramic gap and a transformer housing as used as an image current pass and shielding against external magnetic fields is shown. Right: The technical drawing for a transformer arrangement surrounding a beam pipe including the gap and magnetic shield is shown.

An additional general point is that close to the transformer the electrical conductivity of the beam pipe has to be interrupted as schematically shown in Fig. 5. This is done with an insulator, either a ceramic gap or a plastic vacuum seal. The reason is to prevent a flow of image current inside of the transformer torus. This image current has the opposite sign and without the gap, the fields of the image current and beam current add up to zero. The image current has to be bypassed outside of the transformer torus by some metallic housing. It is surrounded by high permeability μ-metal, also used for the shielding of the transformer against external magnetic fields. A general review on transformers is presented in [9, 10].

Passive transformers or so-called **F**ast **C**urrent **T**ransformers **FCT** are mainly used when beam pulses in a time range from ns to μs have to be observed. The observables are the actual bunch shape, the arrival time with respect to an external reference (e.g. the acceleration frequency) and the total
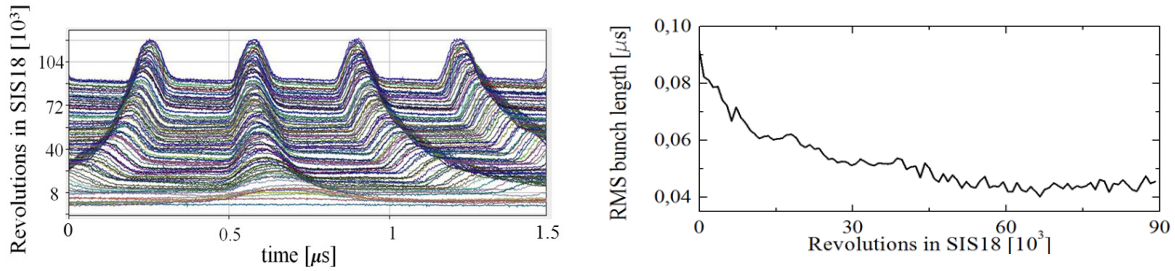
Fig. 6: Left: Signals from a passive transformer installed in GSI synchrotron during the acceleration of a U^{73+} beam. The beam is injected at 11 MeV/u, corresponding to a velocity of $\beta = 15\,\%$ then four bunches are build and accelerated to 350 MeV/u, corresponding to $\beta = 69\,\%$ with an accelerating frequency swing from 0.85 MHz to 3.80 MHz within 0.3 s. Each 0.15 ms a trace of the circulating bunches are shown. Right: The width (one standard deviation) of the bunches during acceleration is shown.

amount of particles gained by the integration of the signal. The bunch structure can be observed with a bandwidth typically 1 GHz, corresponding to a rise time constant of $\tau_{rise} = 160$ ps [8, 11]. As an example the observation of the bunch structure during acceleration inside a synchrotron is shown in Fig. 6 for the acceleration of an ion beam injected at a non-relativistic velocity of $\beta = 15\,\%$ of velocity of light and accelerated to $\beta = 69\,\%$. Due to the increase of the velocity, the bunches approach each other and get smaller as expected from the conservation of the normalized longitudinal emittance, see Section 6. Generally, the observation of the bunches during acceleration and possible bunch merging or splitting is observed by the FCT and eventually a feedback system for the control of the acceleration frequency, amplitude and phase is generated from the FCT signal. An innovative diagnostics method has been developed [12, 13] to determine the longitudinal phase space distribution and hence the longitudinal emittance from a measurement of the bunch shape on a turn-by-turn basis. The idea is based on the tomographic reconstruction used as an imaging technique in medicine for X-ray tomography.

Further types of current transformers exist to adapt the signal output to the time dependent beam structure by dedicate electrical processing: For very short beam pulses in much below 1 ns the signal is integrated by special transformer arrangements by the so-called **I**ntegrating **C**urrent **T**ransformer **ICT**, while for long pulses above 10 μs the so-called **A**lternating **C**urrent **T**ransformer **ACT** are used; their proerties are discussed in Refs. [3, 4, 7, 9, 10]

2.2 The dc-transformer

The transformers discussed in the previous sections only work for a pulsed beam. An essential task for beam diagnostics is the measurement of a coasting beam current (so-called direct current dc beam). The application is either a LINAC producing beam permanently (so-called continuous-wave cw-mode) or a synchrotron with storage times from seconds to many hours.

The principle of a dc transformer, the so-called **D**irect **C**urrent **C**urrent **T**ransformer **DCCT** [8–11] is shown schematically in Fig. 7. It consists of two tori with three types of windings: The first windings of each torus with opposite orientation are used as a modulator. The modulation frequency is typically 1-10 kHz. The amplitude of the modulation current is high enough to force the torus into magnetic saturation of $B_{sat} \simeq 0.6$ T, for positive and negative azimuthal orientation each period. The secondary windings with equal orientation act as a detector for the modulated signal, see Fig. 8. Assuming perfectly identical magnetic characteristics of both tori, the detector signal, as shown in the scheme, should be exactly zero if there is no beam current flowing through the tori. However, an asymmetric shifting of the hysteresis curve results if a dc-beam is fed through the toroids, because of the additional magnetic field from the beam. The sum signal U_S is different from zero with a modulation twice the modulation frequency. In the demodulator stage, this signal is rectified. The dc-current is measured utilizing the cur-
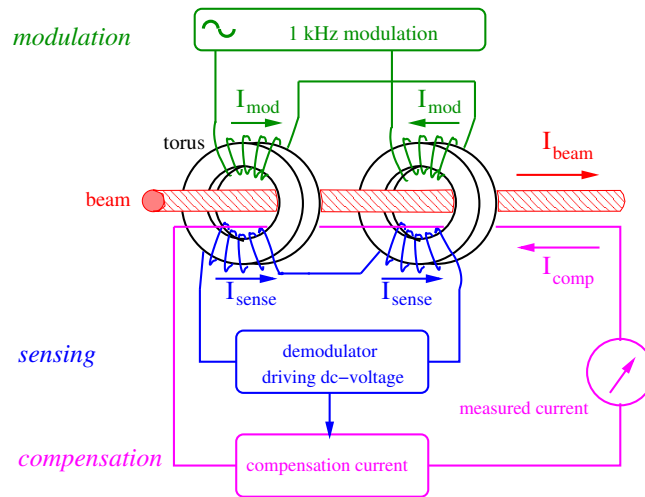
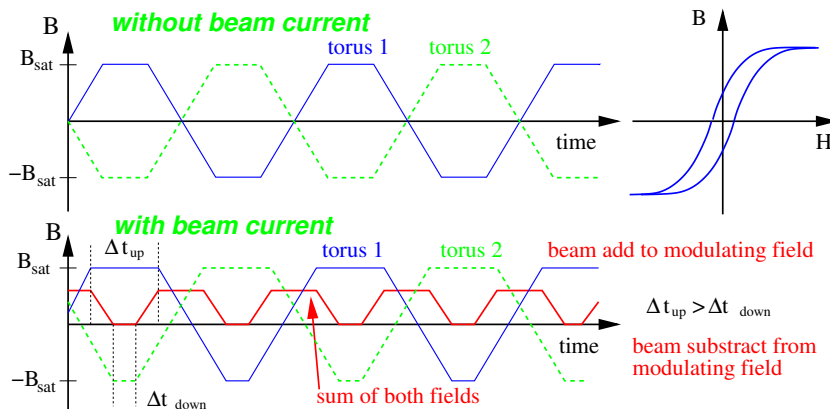**Fig. 7:** Schematics of a dc-transformer, see text.

Fig. 8: The fluxes in the two tori of a dc-transformer without and with a beam. The magnetic field of the beam adds to the modulated field for one modulation phase and 180° degree later it is subtracted. The sum of the maximum magnetization gives the measured signal. The scheme is drawn for a triangular-modulation, for a realistic sine-modulation the edges are smoother.
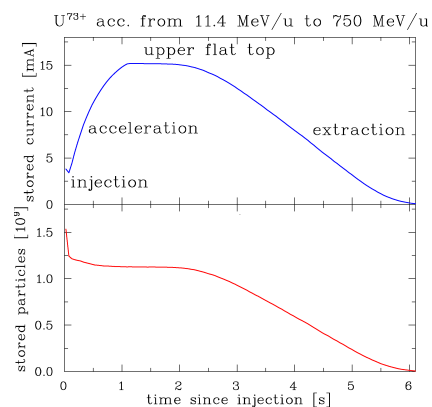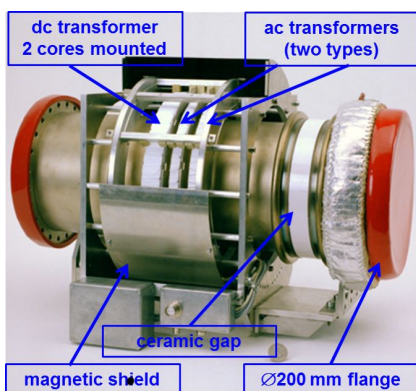

Fig. 9: Left: The dc-transformer installed at the GSI synchrotron. The left torus is the dc-transformer (two tori mounted closely together), further types transformers are installed in this chamber. Right: The signal of a dc-transformer for a $^{238}U^{73+}$ beam at the GSI synchrotron. The electrical current is shown at the top and the number of stored particles at the bottom. The acceleration needs about 1 s. After a delay of about 0.5 s, the slow extraction of 4 s length follows.

Table 2: The specification of the dc-transformer installed at the GSI synchrotron [11].

Parameter	Value
Torus radii	$r_i = 135$ mm, $r_o = 145$mm
Torus thickness l	10 mm
Torus material	Vitrovac 6025: $(CoFe)_{70\%}(MoSiB)_{30\%}$
Torus permeability	$\mu_r \simeq 10^5$
Isolating gap	Al_2O_3
Number of windings N	16 for modulation and sensing
	12 for feedback
Ranges for beam current	300 μA to 1 A
Current resolution I_{min}	1 μA
Bandwidth	dc to 20 kHz
Rise time constant τ_{rise}	20 μs
Offset compensation	± 2.5 μA in auto mode
	< 15 μA/day in free run
Temperature coeff.	1.5 μA/^{o}C

rent generated in the feedback compensation circuit, which forces the output signal back to zero flowing through the third winding of both tori. The detector can even be used at even harmonics of the modulation frequency, which results in higher sensitivity and improvement of the signal-to-noise ratio.

The specification of a typical dc-transformer developed for the heavy-ion synchrotron at GSI is given in Table 2 and a photo in Fig. 9. The resolution is about 1 μA. The offset drift, mainly caused by the magnetic properties of the tori, is of the order of 20 μA per day. The offset can be improved by an automatic zero compensation at times the synchrotron does not contain any beam, e.g., after the ramp down phase of the magnets. For the parameters of the commercially available type see [8].

An example of a dc-transformer measurement is shown in Fig. 9. The electrical current and the number of stored particles are shown. A $^{238}U^{73+}$ beam is injected in the synchrotron, and the acceleration starts shortly after the injection. A loss of particles is seen during the rf bunching process due to some misalignment. During the acceleration the slope of the magnetic field $dB/dt = 1.3$ T/s is constant, resulting in a constant rise of of the particle momentum. The current grows linearly only for non-relativistic velocities due to the decrease of the revolution time, inversely proportional to the velocity. For the maximal energy of 750 MeV/u, corresponding to $\beta = 84$ %, the relativistic increase of the mass starts to be significant. After reaching the maximum energy, a ~ 0.5 s flat top is seen for the de-bunching phase followed by the slow extraction.

2.3 Energy loss and ranges of particles in matter

2.3.1 Material interaction of protons and ions

For the discussion for all intercepting diagnostics like Faraday cups, wire scanners, SEM-grids etc., the energy loss and the related range of the particles penetrating matter serves as the basic physical mechanism. The energy loss of a proton or an ion is mainly due to the collision of the projectile with the electrons within solid target, the so-called electronic stopping power. Due to the different masses of the ion and the electron, the energy transfer to the electron per collision is, in most cases, below 100 eV. The electronic stopping power $\frac{dE}{dx}$ can be approximated by the semi-classical Bethe-Bloch formula which is written in its simplest from as [14–18]

$$-\frac{dE}{dx} = 4\pi N_A r_e^2 m_e c^2 \cdot \frac{Z_t}{A_t}\rho \cdot \frac{Z_p^2}{\beta^2} \left[\ln \frac{2m_e c^2 \gamma^2 \beta^2}{I} - \beta^2 \right] \quad (12)$$
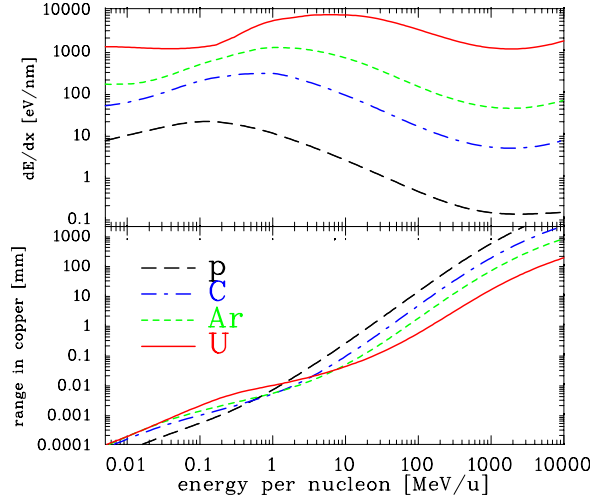
Fig. 10: The energy loss at the surface and the range in copper as a function of the kinetic energy for several ions. The energy range is plotted from 5 keV/u to 10 GeV/u and the range from 100 nm to 1 m. The calculation of the electronic and nuclear stopping uses the semi-empirical code SRIM [17].

with the constants: N_A the Avogadro number, m_e and r_e the mass and classical radius of an electron and c the velocity of light. The target parameters are: ρ density of the target with nuclear mass A_t and nuclear charge Z_t; the quantity $\frac{Z_t}{A_t}\rho$ correspond to the electron density. I is the mean ionization potential for removing one electron from the target atoms; a rough approximation for a target with nuclear charge Z is $I \simeq Z \cdot 10$ eV, more precise values are given e.g. in [17]. The projectile parameters are: Z_p nuclear charge of the ion with velocity β and Lorentz factor $\gamma = (1 - \beta^2)^{-1/2}$. This formula has to be modified since ions travelling through matter are not bare nuclei, but have some inner electrons. An effective charge is used instead of Z_p calculated by e.g. semi-empirical methods described for the codes SRIM [17] or LISE++ [19]. The result of such semi-empirical calculation for the energy loss is shown in Fig. 10 for different ions into copper. The energy loss is maximal for ions with kinetic energy around 100 keV/u to 7 MeV/u (corresponding to velocities $\beta \sim 1.5$ % to 12 %) depending on the ion species. These are typical energies of a proton/heavy ion LINAC. Below 100 keV/u the energy loss decreases and nuclear stopping becomes significant. Energies below 10 keV/u are typical for proton/heavy ion sources mounted on a high voltage platform. For relativistic energies above 1 GeV/u, the energy loss is nearly constant; these are typical energies of particles extracted from a synchrotron.

For the consideration of a Faraday cup (see section 2.4), the range in the material is important. Copper is often used for cups, due to its high heat conductivity. For a particle accelerated to E_{kin}, the range R is calculated numerically from the stopping power via

$$R = \int_0^{E_{kin}} \left(\frac{\mathrm{d}E}{\mathrm{d}x}\right)^{-1} \mathrm{d}E \qquad (13)$$

and has an approximately scaling for ions above $\simeq 10$ MeV/u [14]

$$R \propto E_{kin}^{1.75} . \qquad (14)$$

The results are shown in Fig. 10. This range should be shorter than the mechanical dimension for a practical Faraday cup design; for energies below 100 MeV/u the range is less than 1 cm. Or, in other words, cups are only useful at LINACs or cyclotrons. For higher energies, the range is too large for the typical beam instrumentation sizes and other techniques, e.g. particle detectors are applied. Moreover, at those particles energies are above the nuclear Coulomb barrier where nuclear reactions are possible and charged secondary particles might leave the material resulting in a wrong reading.
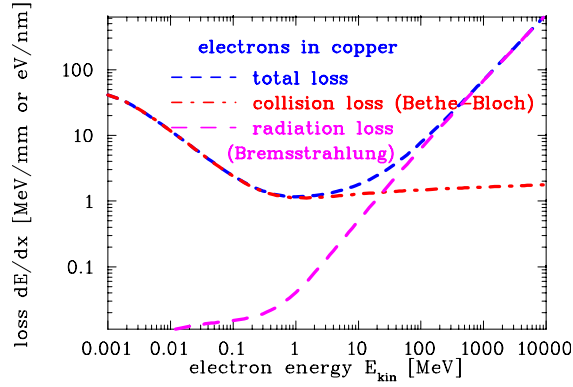
Fig. 11: The energy loss of electrons in copper for collision loss as given by the Bethe-Bloch equation and radiation losses as dominated by the emission of Bremsstrahlungs-photons, data from [21].

2.3.2 Material interaction of electrons

The stopping of electrons in matter differs from protons and ions, see Fig. 11 where the sum of the two relevant processes of collisional loss $dE/dx|_{col}$ and radiation loss $dE/dx|_{rad}$ are added. The collisional loss for electrons due to electronic stopping $dE/dx|_{col}$ is also described by a modified Bethe-Bloch formula; the modification is caused by the equal mass of the projectile and the target electrons and their indistinguishably, see e.g. [18]. This regime dominates only for energies below below 1 MeV as corresponding to the a velocity of $\beta = v/c = 94$ % and a Lorentz-factor of $\gamma = \left(1 - \beta^2\right)^{-1/2} = 2.96$. Even a small electron accelerator reaches higher final energies. For energies above a few 10 MeV the radiation loss by Bremsstrahlung, i.e. the emission of photons by acceleration or deceleration of an electron in the vicinity of the target nucleus, dominant, see e.g. [14]. This radiation loss scales roughly linear to the electron energy and quadratically to the target charge Z_t as $dE/dx|_{rad} \propto E \cdot Z_t^2$. The trajectories of the primary electrons in the target are more curved than for ions, due to the possible high energy- and momentum transfer in a single collision, therefore electrons have much larger lateral straggling than ions. Moreover, the longitudinal straggling is more substantial than for ions resulting in a broader range distribution.

At electron accelerators, Faraday cups are mainly used behind the electron gun for electrons with typically 100 keV energy. In this case, the construction is comparable to the Faraday cups used for proton beams, see Section 2.4. At higher energies, the required amount of material to stop the electrons and to absorb secondary charged particles (e.g $e^+ - e^-$ pair production from the Bremsstrahlungs-photons) increases significantly. A Faraday cup used for high energies up to some GeV is desribed in [20].

2.3.3 Secondary electron generation

When a charged particle, either an ion or an electron, travels through matter it interacts with the target electrons as schematically depicted in Fig. 12 left. In a close, primary collision the target electron can be accelerated to high energies much larger than 100 eV, sometimes these electrons are called δ-rays. The energy distribution depends on the impact parameter and the energy of the incoming particle. In a metallic solid-state material the fast δ-electrons collide with the surrounding electrons; because both collision partners have equal masses the energy is transferred efficiently and more electrons are liberated, see the schematics in Fig. 12. This so-called thermalization of the electrons inside the conduction band is performed in a typical scattering length of $L_s \simeq 10$ nm, i.e. within the distance of some 100 lattice planes. Due to this many collisions, there is only a weak correlation between the direction of the incoming particle and the scattered electrons. If these electrons reach the surface and have still an energy higher than the work-function (typically 1 to 5 eV) they have a high probability to escape from the metal.
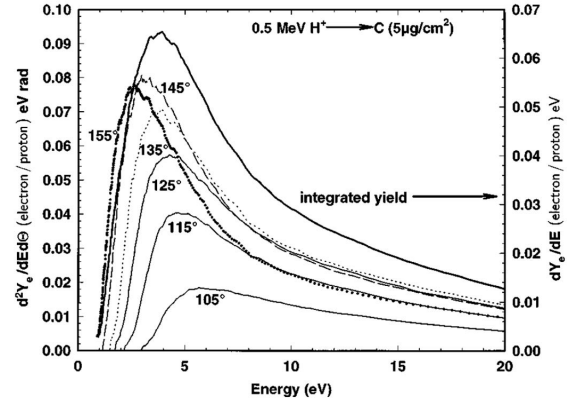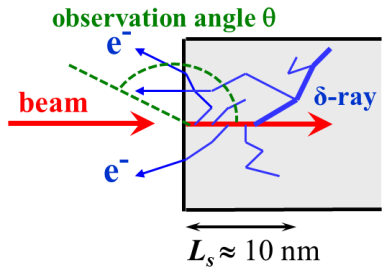
Fig. 12: Left: Schematic drawing of the secondary electron generation from a surface by charged particle impact; L_s is the scattering length from which electrons are able to reach the surface. Right: A typical measurement of the electron energy spectrum for different emission angles and the total yield in backward direction by 0.5 MeV proton impact on a carbon foil [22].

The current of the secondary electrons is given by the so-called Sternglass formula [23]

$$I_{sec} = Y \cdot \frac{\mathrm{d}E}{\rho \mathrm{d}x} \cdot I_{beam} \tag{15}$$

with I_{beam} being the current of incoming particles and Y being the yield factor describing the amount of secondary emission per unit of energy loss $\frac{dE}{\rho dx}$ at the surface of the metal. The yield Y depends on the metal (via the work-function) and the surface quality, e.g. modified by possible adsorbed gas contamination. The mean kinetic energy of the escaping secondary electrons is in the order of 10 eV and has some dependence on the emission angle; an example for the energy spectrum is shown in Fig. 12 and discussed in more details in [22]. To first order the angular distribution $P(\theta)$ of the electron emission can be approximated by a $P(\theta) \propto \cos\theta$ law, where θ is the angle of the trajectory with respect to the surface ($\theta = 180^o$ means backscattering).
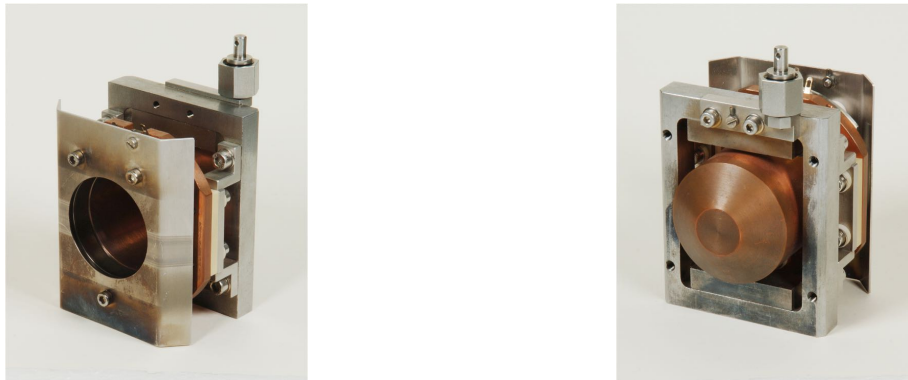
2.4 Faraday cups

A Faraday cup is a beam stopper supposed to measure the electrical current of the beam. The basic cup design is shown in Fig. 13 and a photo in Fig. 14: An isolated metal cup is connected to a current sensitive pre-amplifier. As shown for an active beam transformer, the pre-amplifier consist of a low impedance input and a conversion to a voltage. Range switching is achieved by using different feedback resistors for the operational-amplifier. With a Faraday cup, much lower currents can be measured as compared to a transformer: A measurement of 10 pA for a dc-beam is possible with a low noise current-to-voltage amplifier and careful mechanical design; this is 5 orders of magnitude more sensitive than a dc-transformer. Low current measurement is important, e.g., for the acceleration of radioactive beams.

When an accelerated particle hits a surface, secondary electrons are liberated, see Section 2.3.3. The flux of these electrons are proportional to $\cos\theta$, where θ is the angle of the electron trajectory with respect to the surface; their average energy is below $\simeq 10$ eV. If these electrons leave the insulated cup, the reading of the beam current is wrong by this amount. A secondary electron suppression has to be foreseen. It can be realized by:

– Using a high voltage suppression close to the entrance of the cup. By applying a voltage well above the mean energy of the secondary electrons, they are pushed back to the cup surface, see Fig. 15, left. The disadvantage of this method is related to the fact that the electrical field on the beam axis is lower than on the edges; in the depicted case the maximum potential is about 35 % of the potential applied to the electrode. The emission of the maximal energetic electrons occurred opposite to
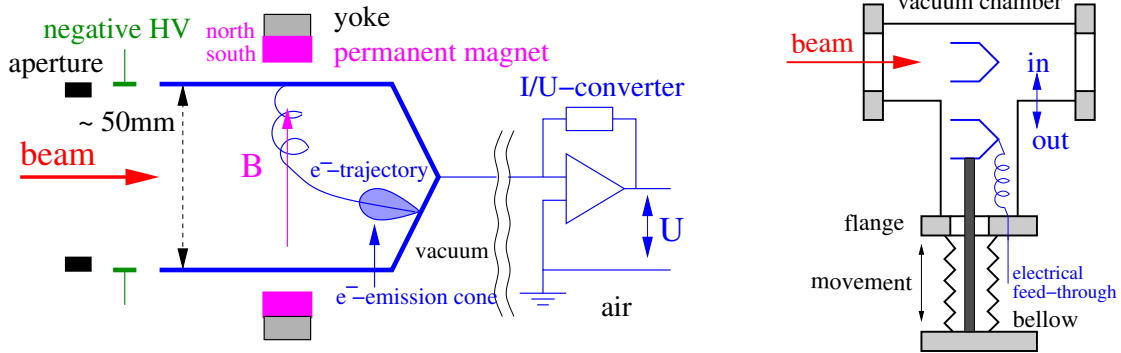
Fig. 13: Left: Scheme of an un-cooled Faraday cup with magnetic and electric secondary electron suppression. Right: Scheme for inside and outside position of destructive diagnostics devices.


Fig. 14: Photo of an Ø50 mm uncooled Faraday cup with magnetic and electric secondary electron suppression.
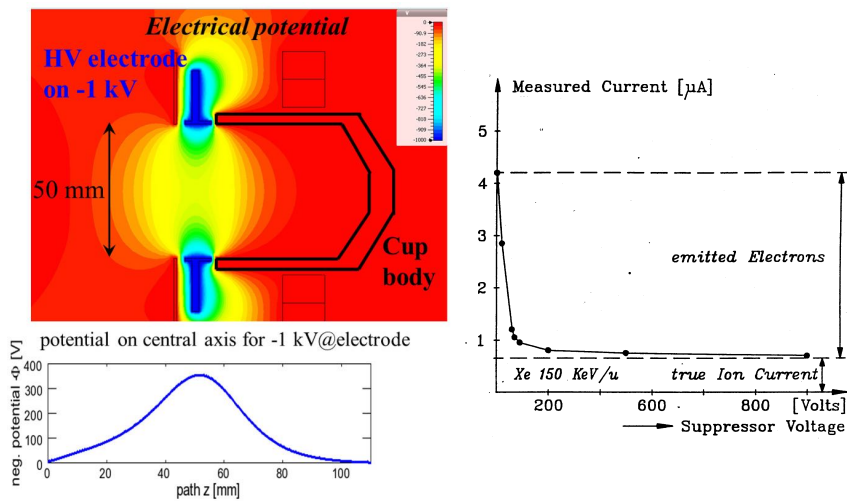
Fig. 15: Left: The electric potential of the Faraday cup as shown in Fig. 14 with the high voltage electrode biased by -1 kV is shown at the cylindrical symmetry plane. The beam enters from left. The negative potential along the central axis is depicted at the bottom. Right: The effect of secondary electrons suppression inside a Faraday cup as determined by the beam current determination a function of the applied voltage.
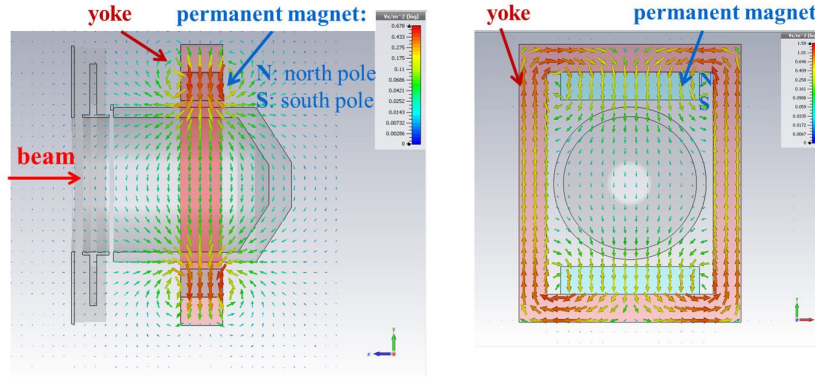
Fig. 16: Magnetic field lines of the arrangement of Co-Sm permanent magnets within the yoke for the Faraday cup of Fig. 14. The homogeneous field strength is $B \sim 60$ mT.

the beam direction, and the potential has to be chosen to be higher than the kinetic energy of at least 99 % of the electrons. A measurement with varying suppression voltage is shown in Fig. 15, right.

– By using a magnetic field created by permanent magnets. In this field B, the secondary electrons spiral around the magnetic field lines with the cyclotron radius r_c

$$r_c = \frac{\sqrt{2m_e E_{kin,\perp}}}{eB} \tag{16}$$

with m_e the electron mass, e its charge and $E_{kin,\perp}$ the kinetic energy of the velocity component perpendicular to the field lines. For the example of $E_{kin,\perp} = 10$ eV and a field of 10 mT the radius is $r_c \sim 1$ mm. With permanent magnets, field lines perpendicular to the beam axis can be created by permanent magnets, see Fig. 16.

3 Beam position monitors

The position of a beam in terms of its transverse centre is very frequently displayed as determined by pick-up plates in a non-invasive manner. It is measure by insulated metal plates where an image current is induced by the electro-magnetic field of the beam particles, see Fig. 17. Because the electric field of a bunched beam is time-dependent, an ac signal is seen on the plate, and the coupling is done using rf technologies. Only time-varying signals can be detected by this principle as generated by a bunched beam. The principle signal shape, as well as the most often used types of pick-ups, are described. The application is the determination of the beam position, i.e. the transverse centre-of-mass of the bunches. To this end, four pick-up plates are installed, and the difference of the signals yields the centre-of-mass in both transverse axes. The device of the plates is called **P**ick-**U**p **PU** the corresponding installation for the centre-of-mass determination is referred as **B**eam **P**osition **M**onitor **BPM**. Various measurements based on this position information are possible but are only discussed briefly at the end of this section.

3.1 Signal treatment of capacitive pick-ups

As shown in Fig. 18, a capacitive pick-up consists of an electrode inserted in the beam pipe. Here the induced image charge of the beam is coupled via an amplifier for further processing. The electrode at a distance a from the beam centre has an area of A and a length in longitudinal direction of l. As the signal we measure the voltage $U_{im}(\omega)$ at a resistor R in the equivalent circuit of Fig. 18 as realized by the input matching of an amplifier or the ADC input. We use the formula in frequency domain
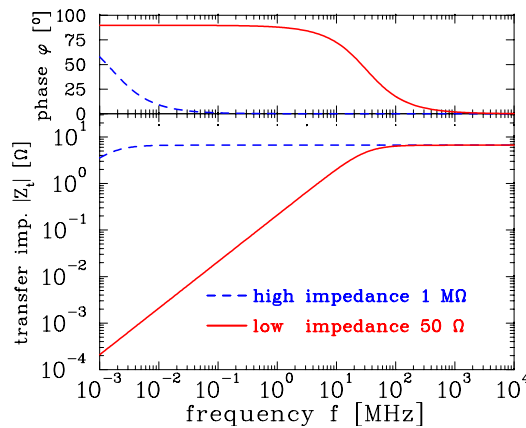
$$U_{im}(\omega) = R \cdot I_{im}(\omega) = Z_t(\omega, \beta) \cdot I_{beam}(\omega) \quad . \tag{17}$$
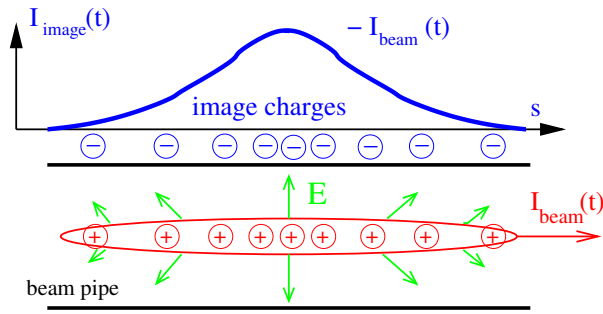
Fig. 17: The beam current induces a wall current of the same magnitude and time structure but reversed polarity.
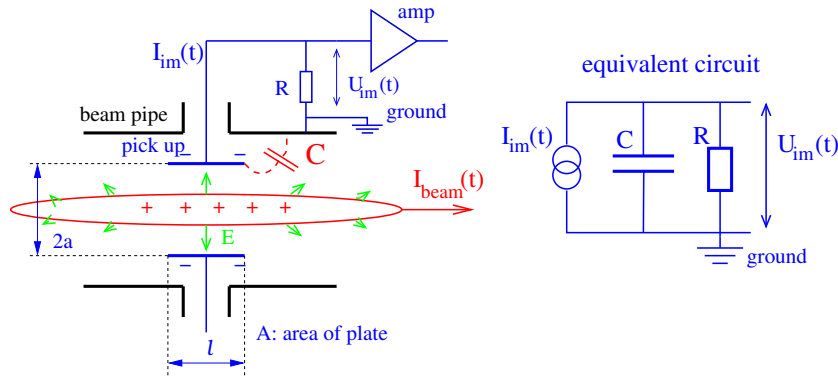

Fig. 18: Scheme of a pick-up electrode and its equivalent circuit.

Fig. 19: Absolute value and phase of the transfer impedance for a $l = 10$ cm long cylindrical pick-up with a capacitance of $C = 100$ pF and an ion velocity of $\beta = 50\%$ for high (1 MΩ) and low (50 Ω) input impedance of the amplifier.

For all types of pick-up electrodes, the general quantity of transfer impedance $Z_t(\omega, \beta)$ is defined by Eq. (17) in the frequency domain according to Ohm's law. The transfer impedance describes the effect of the beam on the pick-up voltage and it is dependent on frequency, on the velocity of the beam particles β and on geometrical factors. It is very helpful to make the description in the frequency domain, where the independent variable is the angular frequency ω, related to the time domain by Fourier transformation. The exact treatment of the signal is discussed in the literature, in particular in Refs. [1–4, 7, 24, 25]; here we discuss only the results.

The transfer impedance is a complex (in the mathematical sense) function for a electrode of the given geometry defined in Fig. 18 with a capacitance C for the signal recording with an input
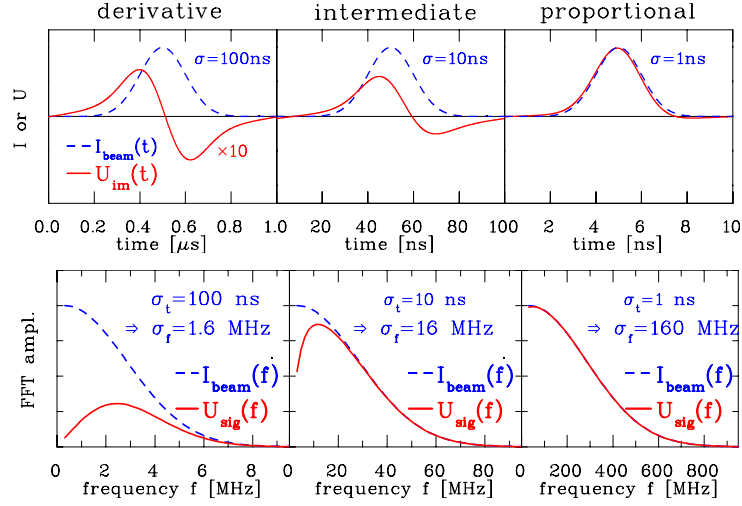
Fig. 20: Simulation of the image voltage $U_{im}(t)$ for the values of the pick-up used in Fig. 19 terminated with $R = 50\,\Omega$ for three different bunch lengths of Gaussian distribution with σ of 100 ns, 10 ns and 1 ns, respectively. The cut-off frequency f_{cut} is 32 MHz. Note the different time scales. (The bunch length in the last case is artificially short for a proton synchrotron.) A Gaussian function in time domain of width of σ_t has a Fourier transformation described by a Gaussian function of width $\sigma_f = 1/(2\pi\sigma_t)$ centred at $f = 0$.

impedance of R as

$$Z_t(\omega, \beta) = \frac{1}{\beta c} \cdot \frac{1}{C} \cdot \frac{A}{2\pi a} \cdot \frac{i\omega RC}{1 + i\omega RC} \quad . \tag{18}$$

This is a description of a first-order high-pass filter for the transfer impedance $Z_t(\omega, \beta)$ with a cut-off frequency $f_{cut} = \omega_{cut}/2\pi = (2\pi RC)^{-1}$. For the case of the so called linear-cut electrodes used at proton synchrotrons (see Section 3.4), a typical value of the capacitance is $C = 100$ pF with a length of $l = 10$ cm. The high-pass characteristic is shown in Fig. 19 for a 50 Ω and a high impedance 1 MΩ amplifier input resistor. In the figure the absolute value

$$|Z_t(\omega)| = \frac{1}{\beta c} \cdot \frac{1}{C} \cdot \frac{A}{2\pi a} \cdot \frac{\omega/\omega_{cut}}{\sqrt{1 + \omega^2/\omega_{cut}^2}} \quad \text{and the phase relation} \quad \varphi(\omega) = \arctan\left(\omega_{cut}/\omega\right) \tag{19}$$

is shown. A pick-up has to match the interesting frequency range, which is given by the accelerating frequency and the bunch length. In a proton synchrotron typical values of the accelerating frequency are in the range from 1-10 MHz, while for LINACs and electron synchrotrons typically 100 MHz to 3 GHz are used.

We can distinguish two extreme cases for the transfer impedance of Eq. (18):

– *High frequency range* $\omega \gg \omega_{cut}$: Here the transfer impedance converges to

$$Z_t(\omega) \propto \frac{i\omega/\omega_{cut}}{1 + i\omega/\omega_{cut}} \longrightarrow 1. \tag{20}$$

The resulting voltage drop at R is for this case

$$U_{im}(t) = \frac{1}{\beta cC} \cdot \frac{A}{2\pi a} \cdot I_{beam}(t). \tag{21}$$

Therefore the pick-up signal is a direct image of the bunch time structure with no phase shift, i.e. $\varphi = 0$. To get a low cut-off frequency $\omega_{cut} = 1/RC$, high impedance input resistors are used to monitor long bunches, e.g. in a proton synchrotron. The calculated signal shape is shown in

694
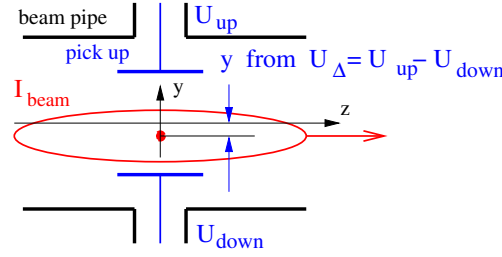
Fig. 21: Schematics of a BPM for the vertical position reading based on the proximity effect.

Fig. 20 (right). Note that in the figure a 50 Ω termination is considered, leading to a large value of the cut-off frequency $f_{cut} = 32$ MHz. In the application of a proton synchrotron, high impedance (~ 1 MΩ) termination yielding a much lower value of the cut-off frequency $f_{cut} = 10$ kHz in this case as shown in Fig. 19 where the condition corresponds to the enlarged flat part of the depicted transfer impedance.

– *Low frequency range $\omega \ll \omega_{cut}$:* The transfer impedance is here

$$Z_t(\omega) \propto \frac{i\omega/\omega_{cut}}{1 + i\omega/\omega_{cut}} \longrightarrow i\frac{\omega}{\omega_{cut}}. \tag{22}$$

Therefore the voltage across R is in this case

$$U_{im}(t) = \frac{R}{\beta c} \cdot \frac{A}{2\pi a} \cdot i\omega I_{beam} = -\frac{R}{\beta c} \cdot \frac{A}{2\pi a} \cdot \frac{\mathrm{d}I_{beam}}{\mathrm{d}t} \tag{23}$$

using the frequency domain relation $I_{beam} = I_0 e^{-i\omega t}$. We see that the measured voltage is proportional to the derivative of the beam current. This can also be seen from the phase relation of the high-pass filter in Fig. 19, where a phase shift of 90° corresponds to a derivative. The signal is bipolar, as shown in Fig. 20 (left).

The fact that a pick-up has a high-pass characteristic leads to the fact that dc-beam cannot be detected (dc-beams are available, e.g. behind the ion source or for a transfer line during slow extraction).

### 3.2 Characteristics for position measurement by BPMs

The deviation of the beam centre with respect to the centre of the vacuum chamber is frequently monitored using four isolated plates or buttons by determining the voltage difference $\Delta U_x = U_{right} - U_{left}$ or $\Delta U_y = U_{up} - U_{down}$ of opposite plates. The closer distance to one of the plates leads to a higher induced voltage. This is called the 'proximity effect' and schematically shown in Fig. 21. Normalizing to the total signal $\Sigma U_x = U_{right} + U_{left}$, the horizontal displacement x can be obtained via

$$x = \frac{1}{S_x} \cdot \frac{U_{right} - U_{left}}{U_{right} + U_{left}} = \frac{1}{S_x} \cdot \frac{\Delta U_x}{\Sigma U_x} \quad \text{(horizontal)} \tag{24}$$

which is independent of the beam intensity. For the vertical plane the position y is given by

$$y = \frac{1}{S_y} \cdot \frac{U_{up} - U_{down}}{U_{up} + U_{down}} = \frac{1}{S_y} \cdot \frac{\Delta U_y}{\Sigma U_y} \quad \text{(vertical)}. \tag{25}$$

This position measurement is the most frequent application of pick-ups, hence they are called **B**eam **P**osition **M**onitor **BPM**. The proportional constant S_x respectively S_y between the measured normalized voltage difference and the beam displacement is called position sensitivity and its unit is $S = [\%/\text{mm}]$. Sometimes the inverse is used $k = 1/S$ given in units of $k = [\text{mm}]$ and is called BPM position constant
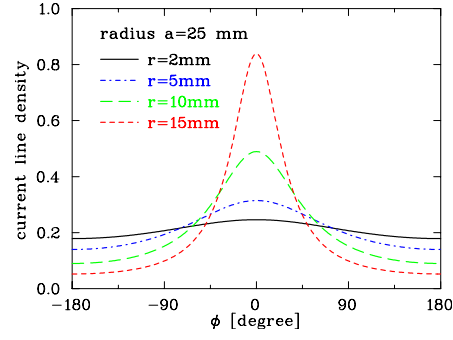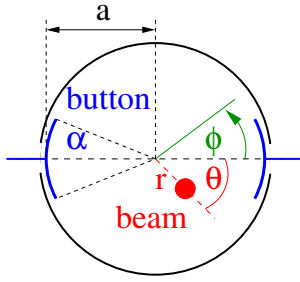
Fig. 22: Schematics for a button BPM and the image current density generated by a 'pencil' beam at different displacements r for an azimuth $\theta = 0$.

or position sensitivity as well. It is possible that the position sensitivity depends on the beam position itself, corresponding to a non-linear voltage response for a large beam displacement and, additionally on the evaluation frequency, hence it is a function $S = S(x, y, \omega)$.

For typical beam displacements less than 1/10 of the beam pipe aperture, the difference ΔU is lower by about this factor compared to the sum voltage ΣU, i.e.,

$$\text{typically} \quad \Delta U \ll \frac{\Sigma U}{10} \quad . \tag{26}$$

Sensitive signal processing is required for the difference voltage to achieve a sufficient signal-to-noise ratio.

3.3 Position measurement using button BPMs

For a round arrangement of buttons, a simple 2-dimensional electro-static model can be used to calculate the voltage difference as a function of beam displacement. According to Fig. 22 we assume a thin, 'pencil' beam having a transverse extension much lower the beam pipe radius of current I_{beam} which is located off-centre by the amount r at an angle θ. The wall current density j_{im} at the beam pipe of radius a is given as a function of the azimuthal angle ϕ as

$$j_{im}(\phi) = \frac{I_{beam}}{2\pi a} \cdot \left(\frac{a^2 - r^2}{a^2 + r^2 - 2ar \cdot \cos(\phi - \theta)} \right) \tag{27}$$

and is depicted in Fig. 22; see [26] for a derivation of this formula.

As discussed above, this represents the proximity effect, where the current density depends on the distance with respect to the beam centre. The button-type BPM electrodes covering an angle α and the image current I_{im} is recorded as given by:

$$I_{im} = a \int_{-\alpha/2}^{+\alpha/2} j_{im}(\phi) d\phi \quad . \tag{28}$$

The resulting signal difference for opposite plates as a function of horizontal beam displacement, corresponding to $\theta = 0^o$, shows a significant non-linear behaviour as displayed in Fig. 23. The signal voltage is calculated according to Eq. (17) as $U = R \cdot I_{im}$. It can be seen that for the normalised difference $\Delta U/\Sigma U$ the linear range continues to a larger beam offsets. The non-linearity increases if the beam centre moves outside the horizontal axis, which is depicted in Fig. 23 for different values of the azimuthal orientation θ as a function of horizontal displacement $x = r \cdot \cos\theta$ according to Eqs. (27) and (28). The non-linearity can be influenced by the button size as represented in this 2-dimensional approach by the angle α. However, in the central part, the reading is nearly independent of the orientation
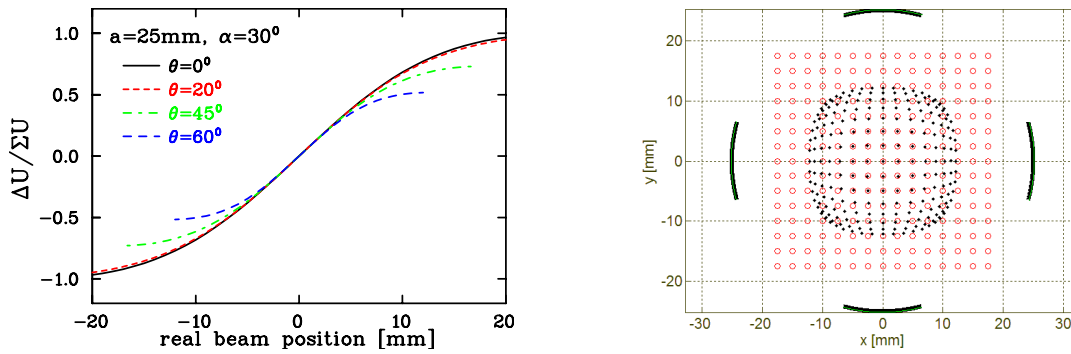
Fig. 23: Left: Horizontal position calculation for different azimuthal beam orientation θ for an BPM electrode arrangement of angular coverage $\alpha = 30^o$ and a beam pipe radius $a = 25$ mm as a function of horizontal beam displacement Right: In the position map the open circles represent the real beam position and the dots are the results of the $1/S \cdot \Delta U/\Sigma U$ algorithm with $S = 7.4$ %/mm for the central part.
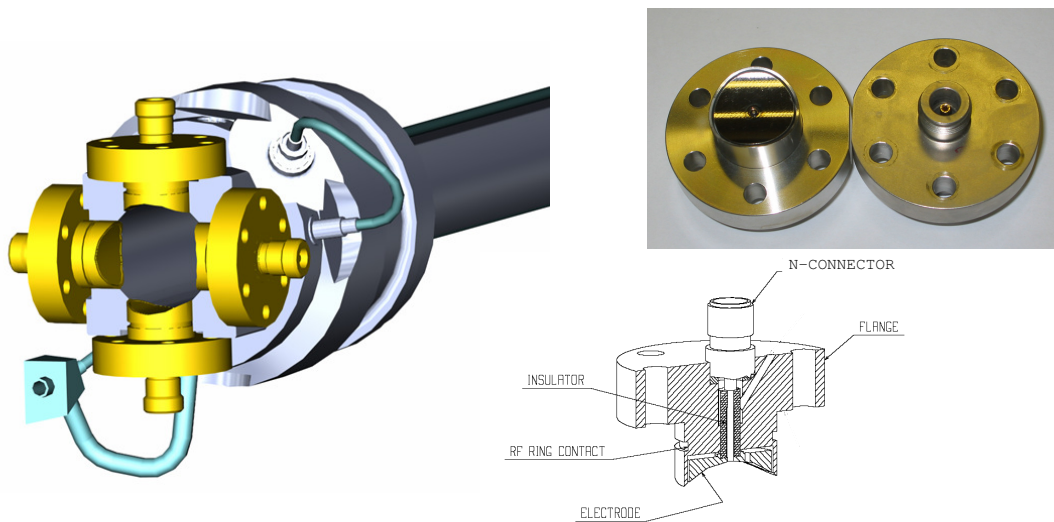

Fig. 24: Left: The installation of the curved Ø 24 mm button BPMs at the LHC beam pipe of Ø 50 mm [27]. Right: Photo of a BPM used at LHC, the air side is equipped with an N-connector as well as a technical drawing for this type.

leading to a universal position sensitivity S. The dependence between the horizontal and vertical plane is better depicted in the position map of Fig. 23, right: Here the real beam positions with equidistant steps are plotted as well as the results using $1/S \cdot \Delta U/\Sigma U$ calculations with S fitted at the central part. The preceding 2-dimensional electro-static model delivers satisfying result for typical electron beams of relativistic beam velocities i.e. TEM-like field pattern; only minor corrections are necessary for the case of a circular pick-up.

A BPM arrangement obeying the circular beam pipe geometry is installed at CERN LHC and depicted in Fig. 24. Due to the size and the round electrodes, this arrangement is commonly called button BPM. The reason for such installation is to ensure a smooth transition from the regular beam pipe to the BPM region and to prevent for excitation of an electro-magnetic field by the beam, the so-called wake-field. In most other cases, planar buttons are used due to their simpler mechanical realisation.

Button pick-ups are the most popular devices for electron accelerators. They consist of a circular plate of typically 10 mm diameter mounted flush with the vacuum chamber. The cross-section of the chamber is not changed by this insertion, to avoid excitation of wake-fields by the beam. The button itself should have a short vacuum feed-through with a smooth transition to the 50 Ω cable, to avoid

697
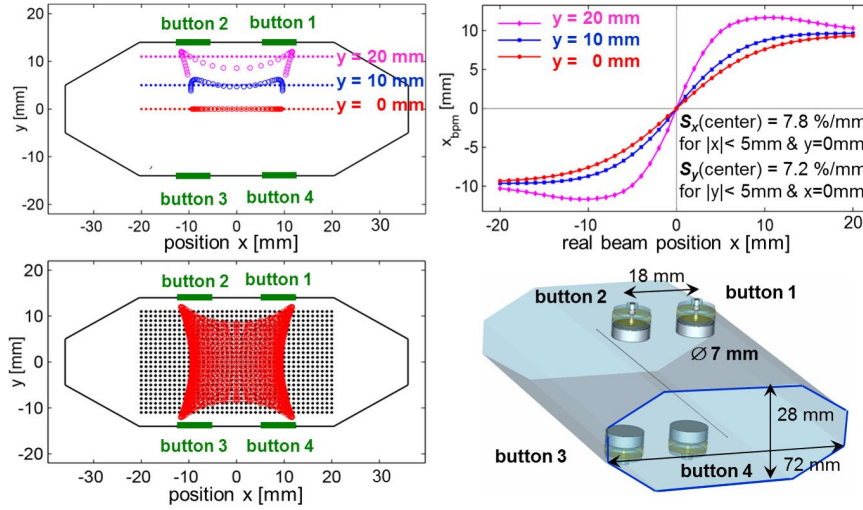
Fig. 25: Numerical calculation of the position map for the arrangement at the synchrotron light source ALBA; from [28]. Top left: Results of position calculation for a horizontal scan from -20 mm $< x < 20$ mm for three vertical offsets using constant horizontal $S_x(center)$ and vertical $S_y(center)$ position sensitivities. Top right: The calculated position for the horizontal scan for these three vertical offsets; the horizontal position sensitivity $S_x(center)$ at the central part is determined from the slope of the curve with zero vertical offset. Bottom left: Position map for the entire horizontal and vertical range. Bottom right: The geometry of the Ø 7 mm button pick-ups of 18 mm horizontal distance within the chamber.

excitation of standing waves and to reach a bandwidth up to 10 GHz.

Fig. 25 shows a typical setup used at the storage ring of a synchrotron light source within a planar arrangement, where the buttons are not mounted in the horizontal plane only to avoid synchrotron light hitting the feed-through. The position is evaluated via

$$\text{horizontal: } x = \frac{1}{S_x} \cdot \frac{(U_1 + U_4) - (U_2 + U_3)}{U_1 + U_2 + U_3 + U_4} \quad \text{vertical: } y = \frac{1}{S_y} \cdot \frac{(U_1 + U_2) - (U_3 + U_4)}{U_1 + U_2 + U_3 + U_4} \quad (29)$$

using all four electrode voltages for the position determination. An appropriate size and location of the buttons for a linear sensitivity within a maximal range at the central part and comparable values of the related horizontal and vertical position sensitivity has to be calculated numerically, see e.g. [28]. The optimised location depends on the size and distances of the electrodes, as well as the chamber cross-section. The inherent geometry of the vacuum chamber leads to a non-linear position sensitivity and a strong coupling between horizontal and vertical displacements (i.e. non-linear position sensitivity $S(x, y)$ in Eq. (24)). In contrast to the circular arrangement, even at the central part the horizontal position sensitivity $S_x(x, y)$ depends significantly on the vertical displacement y as well and a corresponding dependence for the vertical direction $S_y(x, y)$.

3.4 Linear-cut BPMs for proton synchrotron

Related to the long bunches at proton or ion synchrotrons of typically several meters, long electrodes of typically 20 cm are installed to enhance the signal strength. A box-like device is used normally, to get a precise linear dependence with respect to the beam displacement, see Fig. 26. For the previously discussed button pick-up geometries, the signal of the plate closer to the beam's centre-of-mass is larger than that of the more distant plate; this is called the proximity effect. By contrast, the linear-cut BPMs have another principle: The influenced signal is proportional to the actual plate length at the beam centre position. For a given beam displacement x the electrode's image voltage U_{im} is proportional to the length l_{left} and l_{right} of the beam projected on the electrode surface as shown for the horizontal direction in
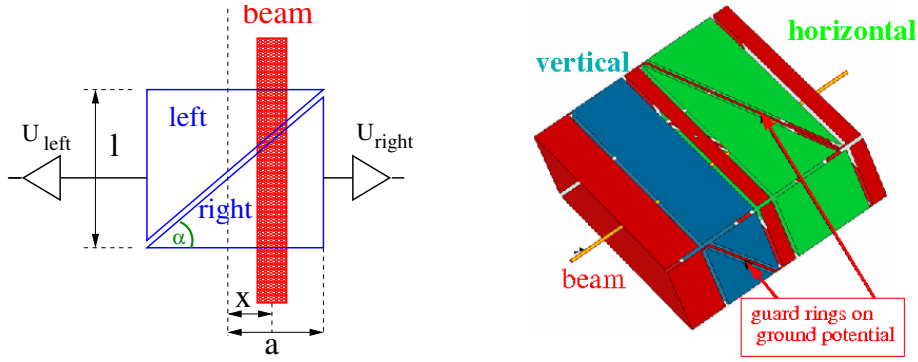
Fig. 26: Left: Scheme of the position measurement using the so-called linear-cut and an example of an electrode arrangement for the horizontal plane. Right: Schematic drawing for a linear-cut BPM for both planes.

Table 3: Simplified comparison between linear-cut and button BPM.

	Linear-cut BPM	**Button BPM**
Precaution	bunches longer than BPM	bunches comparable to BPM
BPM length (typ.)	10 to 20 cm per plane	Ø 0.5 to 5 cm
Shape	rectangular or cut cylinder	orthogonal or planar orientation
Mechanical realization	complex	simple
Coupling	often 1 MΩ, sometimes 50 Ω	50 Ω
Capacitance (typ.)	30 - 100 pF	3 - 10 pF
Cut-off frequency (typ.)	1 kHz for $R = 1\text{M}\Omega$	0.3 to 3 GHz for $R = 50\,\Omega$
Usable bandwidth (typ.)	0.1 to 100 MHz	0.3 to 5 GHz
Linearity	very linear, no x-y coupling	non-linear, x-y coupling
xPosition sensitivity	good	good
Usage	at proton synchrotron, $f_{acc} < 10$ MHz	proton LINAC, all electron acc. $f_{acc} > 100$ MHz

Fig. 26, left. For triangle electrodes with half-aperture a one can write:

$$l_{right} = (a + x) \cdot \tan \alpha \quad \text{and} \quad l_{left} = (a - x) \cdot \tan \alpha \implies x = a \cdot \frac{l_{right} - l_{left}}{l_{right} + l_{left}} \quad . \tag{30}$$

The position reading is linear and can be expressed by the image voltages as

$$x = a \cdot \frac{U_{right} - U_{left}}{U_{right} + U_{left}} \equiv \frac{1}{S_x} \cdot \frac{\Delta U_x}{\Sigma U_x} \implies S_x = \frac{1}{a} \tag{31}$$

which shows that the position sensitivity for this ideal case is simply given by the inverse of the half-aperture. Compared to other types of pick-ups, the position sensitivity is constant for nearly the full range of displacements. Moreover, the position reading in the horizontal plane is independent on the beam position in the vertical plane. Due to the linearity the position reading is independent on the beam size, which is of importance for the relatively large beam size compared to the chamber aperture for low energy proton or ion synchrotrons. This position linearity is the main advantage of the linear-cut type as compared to the button BPM type. As a summary the basic parameters for linear-cut and button BPMs are compared in Table 3.

For the position measurement, other techniques are used in addition: this comprises stripline BPMs working like a directional coupler to separate the signal of counter-propagating beams in a collider. Moreover, monitors are used based on the measurement of the magnetic field by so-called inductive pick-ups or the excitation of cavity modes within a so-called cavity BPM. Further descriptions and citations can be found in Refs. [1–4, 7, 24, 25, 29].
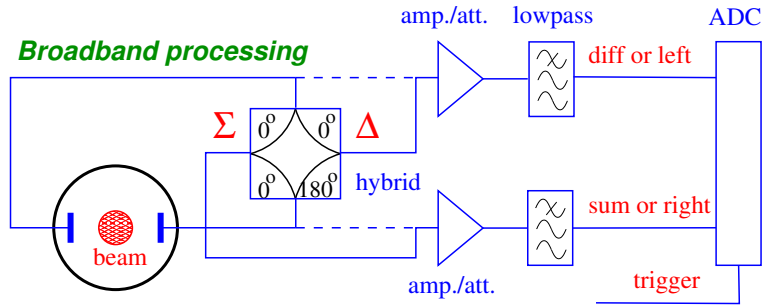
Fig. 27: Scheme of a broadband signal processing. The plate signals are either fed directly to the amplifier (dashed line) or via a hybrid the sum and difference is generated in an analogue manner (solid line).
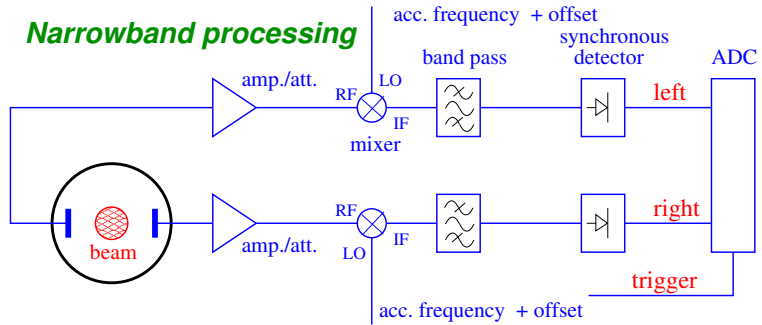

Fig. 28: Schematic signal analysis for a narrow-band treatment.

3.5 Electronic treatment for position determination

To get the position of the beam, the signals from the electrodes have to be compared. For this comparison, the signal shape (differentiation or proportional behaviour) is of minor importance. The electronics used for this purpose are described only briefly in this contribution; a detailed review is given in [1–3, 30, 31]. For the position resolution, the signal-to-noise ratio is amplifier noise, as well as the electronic noise of the following devices contribute. Therefore a minimum bunch current is needed for a reliable position measurement. Two different principles are commonly used based on analogue electronics, the so called broadband and narrow-band processing:

Broad-band processing: In the broadband case, as shown in Fig. 27, the signals from the individual plates are amplified (or even attenuated) to adapt the signal strength to the ADC input level. The sum and difference signal is then calculated from the digitised values. For noise reduction and alias-product suppression, a low-pass filter is used matched to the sample rate of the ADC. In many applications, the sum and difference voltages are analogously generated by a 180° hybrid or a differential transformer. Because they are purely passive devices, they can be mounted quite close to the BPM plates even in case of high radiation. The resulting sum and difference signals are then stored in the ADC. The difference signal, which is usually lower by at least a factor of 10, can be amplified by a higher amount than the sum signal to exploit the full ADC range. The analogue electronics is required to match the signal shape to the properties of the ADC. With the help of high-speed digital signal processing, the bunch signal is then reduced to one value per bunch and the beam position is calculated from the sum and difference value. The precision of this method is lower as compared to the narrow-band processing described below. For electron machines, with small beam size, a resolution of 100 μm can be achieved by this broadband processing. The advantage is the possibility to perform a bunch-by-bunch analysis (i.e. measuring the position of always the same bunch rotating in a synchrotron) by using an appropriate trigger setting or precise digital signal processing. The broadband scheme is installed at transfer lines between synchrotrons where only one or few bunches are transferred.
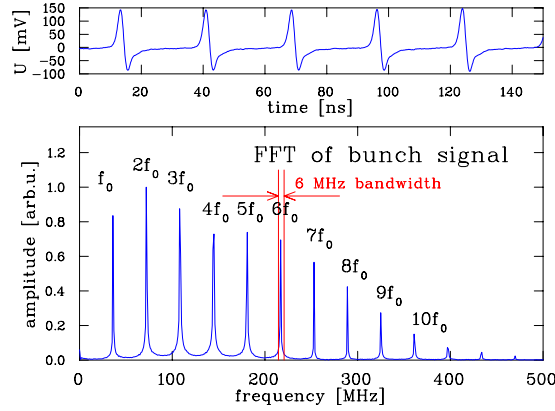
Fig. 29: Bunch signal (top) and its Fourier transformation (bottom) at the GSI-LINAC of a 1.4 MeV/u beam. In the Fourier spectrum each line corresponds to the indicated harmonics of the 36 MHz accelerating frequency. The position evaluation is done at $6f_0 = 216.8$ MHz by a 6 MHz narrow-band processing as indicated by the red lines.

Narrow-band processing: The narrow-band processing is used to get a higher precision of the position reading, attaining 1 μm in electron machines by this electronics scheme. The better signal-to-noise ratio is achieved by reducing the bandwidth of the signal processing by several orders of magnitude. As an illustrative example, the Fourier-Transformation of the signal from the GSI-LINAC pick-up is shown in Fig. 29. The spectral power of the signal is mainly available at the bunch repetition harmonics nf_0. The position evaluation uses only this considerable signal power within the band of frequency span Δf. By this an effective noise reduction is achieved by a limitation of the signal processing bandwidth, because the unavoidable thermal noise voltage U_{eff} at a resistor R scales with the square root of the bandwidth Δf as $U_{eff} = \sqrt{4k_BTR\Delta f}$ with k_B being the Boltzmann constant and T the temperature. Technically, the pick-up signal is mixed with the accelerating frequency using standard rf-components. The resulting quasi-dc signal is then digitised by an ADC, and the position is calculated via software. In general, this technique is called heterodyne mixing, and the same principle is used in a spectrum analyser. The mixing corresponds to an average over many bunches leading to much higher precision in the position reading but does not allow a turn-by-turn observation. Besides for a synchrotron, such narrow-band processing is applied at LINACs or behind cyclotrons with a pulse length above 10 μs. In case only one or few bunches are transferred, e.g. between two synchrotrons, the narrow-band processing cannot be applied.

Motivated by the intensive usage in telecommunication the sampling rate and a voltage resolution of ADCs have significantly improved in the last decades; an overview on ADC technologies can be found in Refs [1, 3]. Modern technologies tend to digitise the signal on an early stage of the signal path and replace the analogue conditioning by digital signal processing, e.g. performing the narrow-band treatment in the digital domain. The related methods compared to the analogue treatment are reviewed in [31].

3.6 Trajectory measurement

With the term trajectory the position of a single bunch during its transport through a transport line or within a synchrotron is meant, and it is the basic information of the initial alignment of the accelerator setting. Because the single bunch position is monitored, a broadband processing for the BPM electronics is used. As an example of a measurement Fig. 30 depicts the measurement of the trajectory of a single bunch injected into the LHC on the first days of its commissioning [32]. The position reading at each of the 530 BPM on the 27 km long synchrotron is displayed showing some oscillations caused by mismatched injection parameters, which could be aligned later on with the help of this diagnostics. To this

respect, the LHC is treated as a transfer line.
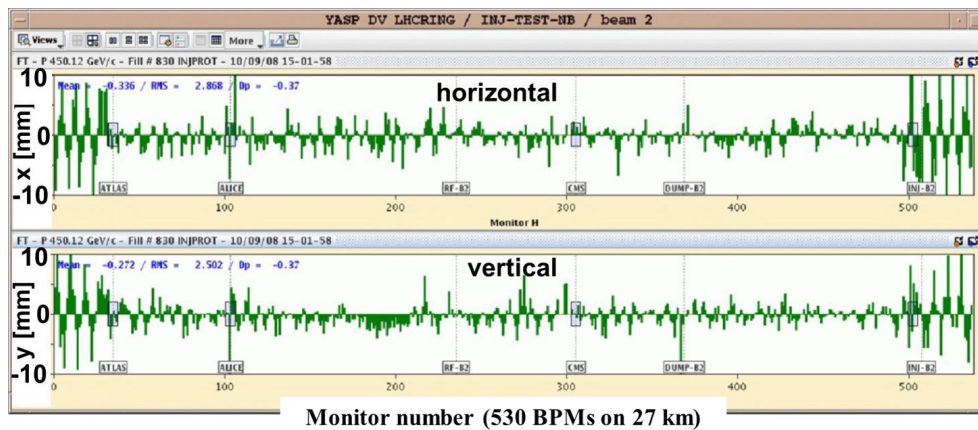
Fig. 30: Measurement of the trajectory of a single bunch injected in the LHC with a position display at the 530 BPMs around the synchrotron [32].

3.7 Closed orbit measurement at a synchrotron

The closed orbit within a synchrotron is measured via the position averaged over many turns; the required accuracy is in the order of 10 μm for proton accelerators and about 1μm for synchrotron light sources with typical averaging duration in the the order of 10 ms. In a synchrotron, several BPMs for the determination of the closed orbit are installed to enable sufficient correction possibilities. An example of the use of a position measurement is displayed in Fig. 31 during the acceleration in the GSI synchrotron.
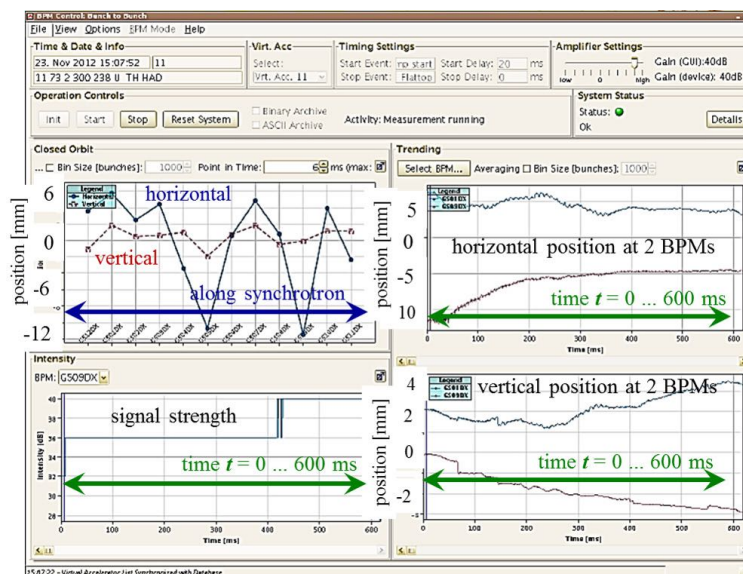
Fig. 31: Example of a position measurement done at the GSI synchrotron for a partly misaligned beam during a 0.6 s long acceleration. The upper left plot shows the position around the ring at 12 locations at the begin of the ramp; the upper right plot shows the horizontal position during the acceleration ramp for two BPM locations, the lower right plot the vertical position for these BPMs; the lower left plot is a signal power $\propto U_\Sigma^2$ during the ramp for a single BPM. The panel at the top is used for the control of pre-amplifiers and timing.

The position reading of the BPMs around the ring can be used as the input of a feedback loop to do an active beam correction to compensate systematic and temporal misalignments, such a feedback system is installed in most synchrotrons, see e.g. [33]. To enable proper automatic corrections, four
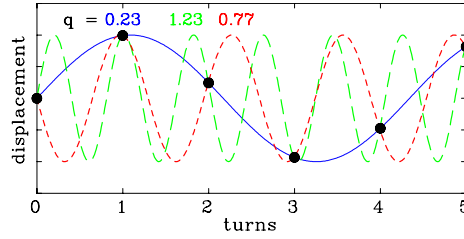
Fig. 32: Schematic of the tune measurement for six subsequent turns determined with one pick-up, together with the three lowest frequency fits.

BPMs per tune value, separated approximately by about $\mu_\beta \simeq 90^o$ betatron phase advance, is a typical choice.

3.8 Tune measurement

One essential parameter of a synchrotron is its tune as given by the amount of betatron oscillations per turn. The principle of a tune measurement is related to excite a coherent transverse betatron oscillation and the position determination by BPMs on a turn-by-turn basis.

The tune value can be split in two parts as $Q = Q_n + q$ with Q_n is the integer part and q fractional part; the measurement determines only the fractional part q. The integer number of oscillations Q_n cannot be seen, but this is normally of no interest, as it is known from calculations. This behaviour is schematically shown in Fig. 32 for the case of a turn-by-turn reading of one BPM: A sine function can be fitted through the position data, but one cannot distinguish between the lowest frequency (here $q = 0.23$) and higher values, leading to the fact that the fractional part is only uniquely defined for $0 < q < 0.5$. To distinguish between a value below or above 0.5, the focusing by the quadruples (i.e. the tune) can be slightly changed and the direction of the shift of q can be observed.

### 3.8.1 The kick method, time-domain method

For this method, coherent betatron oscillations are excited by a fast kick. This kick has to be much shorter than the revolution time $1/f_0$ and is provided in most cases by a so-called kicker magnet. The strength of the kick has to be chosen to prevent for beam losses. The beam position is monitored turn-by-turn (broadband processing only), and it is stored as a function of time. The Fourier transformation of the displacements gives the fractional part q of the tune. An example from the GSI synchrotron is shown in Fig. 33.

To understand the limitation of this method, one has to look at the single particle behaviour. At the time of the kick, the particles start a free betatron oscillation with the same phase, but each particle has a slightly different betatron frequency due to the tune spread. Even if the individual oscillations last for a long time, the coherent motion detected by a pick-up is damped as a consequence of the de-coherence of the individual motion given by the time of the inverse betatron frequency spread, see Fig. 34. To achieve an adequate resolution of typically $\Delta q \simeq 10^{-3}$, at least $N = 500$ turns of non-vanishing displacements are needed. In several practical cases, the de-coherence time is shorter than this border as demonstrated in Fig. 33. Hence, this straightforward method is not very precise.

An additional drawback of such a measurement is a blow-up of the transverse emittance of the stored beam, because the excitation of the individual particles are damped much slower than the coherent motion as depicted in Fig. 34. For proton synchrotrons this can be of relevance, in contrary to electron synchrotrons where the trnasverse particle motion is damped relatively fast by synchrotron radiation.
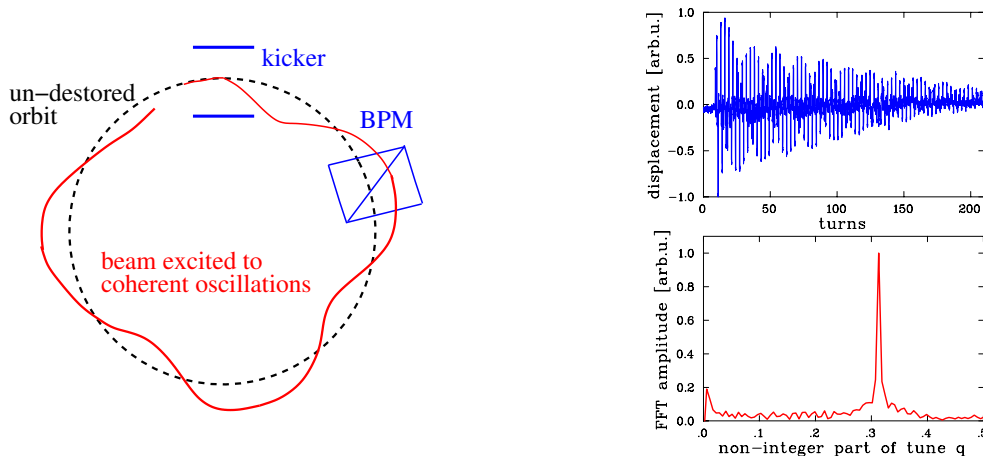
Fig. 33: Left: Scheme of the beam excitation and detection of coherent bunch oscillations by a BPM. Right: Beam oscillations after a kick excitation recorded in the time domain for 200 turns (top) and its Fourier transformation for q determination (bottom) at the GSI synchrotron.
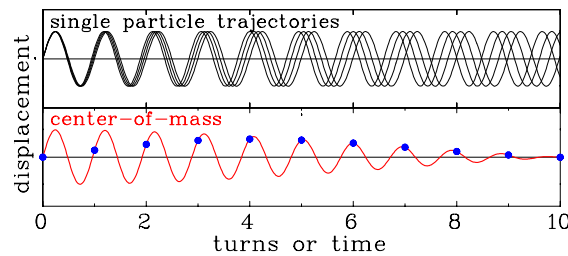
Fig. 34: Plot of the individual trajectories of four particles after a kick (top) and the resulting coherent sum signal as measured by a pick-up (bottom). (The tune spread is much too large for a real machine.)
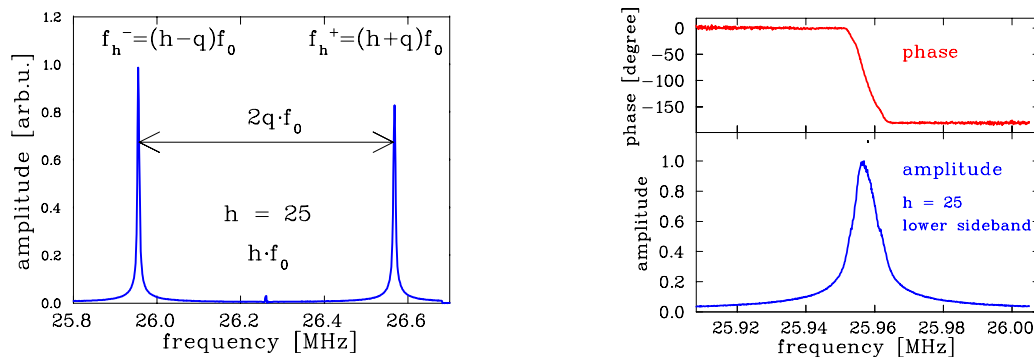
Fig. 35: BTF measurement at the GSI synchrotron with a 500 MeV/u U^{73+} beam having a revolution frequency of $f_0 = 1.048$ MHz. The wide scan around the $h = 25^{th}$-harmonics is shown left and a scan around a lower sideband centred at f_{25}^- on the right for amplitude and phase. The fractional tune is $q = 0.306$ for these data.

3.8.2 *Transverse excitation by a frequency chirp*

For this method, an rf method for tune determination uses a beam excitation driven by a continuous sine wave stimulus. This wave is typically swept slowly within some 100 ms over a certain band, and the response of the beam is measured in coincidence. The displayed spectrum represents the **B**eam **T**ransfer **F**unction **BTF**, which can be defined as the transverse velocity response to the given acceleration by the kicker. Besides the name BTF measurement, this method is sometimes called 'beam excitation by a frequency chirp'.

Due to practical reasons, a harmonics of the revolution frequency f_0 is used for the excitation, and

704
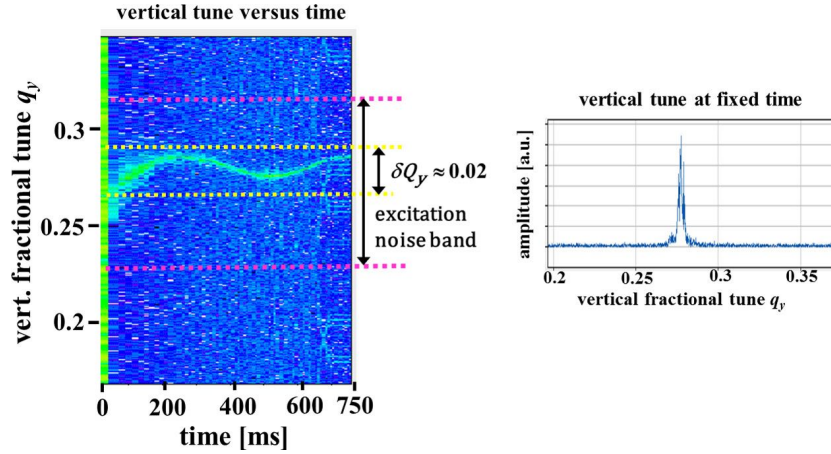
Fig. 36: Left: Measurement of the tune at the GSI synchrotron for an Ar^{10+} beam accelerated from 11 to 300 MeV/u within 0.75 s. Displayed is the Fourier transformation of displacements of successive individual bunches over 4096 turns excited by the depicted noise band during acceleration as a function of time. The maximum of the Fourier transformation is colour-coded in a linear manner. Right: Single tune spectrum 110 ms after the ramp start averaged over 4096 turns corresponding to ~ 15 ms.

the resulting resonance line is expressed in terms of these harmonics. An example of such a measurement with an excitation around the $h = 25^{th}$ revolution harmonics is shown in Fig. 35. The beam reacts as a driven oscillator with a resonance as given by the tune value. Because only the fractional part can be measured, this resonance is located at $f_h^{\pm} = (h \pm q)f_0$ on both sides of the revolution frequency and are called lower and upper sideband. From the distance of the sidebands, the fractional part of the tune q is determined. The resonance nature of the BTF measurement can also be seen from the phase shift of 180° during resonance crossing, as shown in on the right side of Fig. 35. With this method, a high precision of the tune value q up to 10^{-4} can be reached.

3.8.3 *Noise excitation of the beam*

Instead of a single frequency excitation, a wide-band rf signal can be applied: The excitation takes place for all frequencies at the same time, using white noise of adequate bandwidth being larger than the tune variation. The position reading is done in the time domain using a fast ADC recording each bunch. The position data for each bunch are Fourier analysed, and the spectrum is drawn corresponding to the tune value. An example is shown in Fig. 36 from the GSI synchrotron during acceleration. The resolution for the tune is given by the inverse of the averaging time for one Fourier transformation calculation (for the data in Fig. 36 in the order of some ms, corresponding to 4096 turns), leading to about $\Delta Q \sim 3 \cdot 10^{-3}$ for one single scan. Due to the band excitation, a time-resolved observation of the tune is possible during the entire acceleration ramp.

3.9 **Further measurements using BPMs**

Using the results of position measurements at a synchrotron, various beam parameters can be determined; some of them are briefly summarised here:

Chromaticity measurement: The chromaticity ξ is the coupling between the relative momentum offset Δp with respect to the reference particle with momentum p_0 and the tune offset ΔQ according to $\frac{\Delta Q}{Q_0} = \xi \cdot \frac{p}{p_0}$. By a slight momentum change using a detuned rf-frequency, the particles can be slightly accelerated or decelerated. The tune is then measured and plotted as a function of the momentum deviation; the slope gives the value of ξ. More detail related to this advanced beam diagnostics is discussed in the corresponding articles in Refs. [1, 3].

β-function measurement: For the tune measurement, the bunch position at one BPM is read and analysed. As there are many BPMs installed in a synchrotron (as needed for the closed orbit feedback), a measurement can be done following one single bunch position from one BPM to the next while exciting the beam to coherent betatron oscillations. The bunch movement corresponds to the betatron phase advance $\Delta\mu$ from one BPM location at s_0 to the next location s_1. For this the values of the β-function at this location can be calculated with the help of the formula $\Delta\mu = \int_{s0}^{s1} \frac{\mathrm{d}s}{\beta}$ and compared to the expected value from beam optics calculations. The general method, advanced technologies and analysing methods are discussed in [1, 3, 34]

Dispersion measurement: The dispersion $D(s)$ along the accelerator location s is coupling between the relative momentum offset Δp with respect to the reference particle with momentum p_0 and the position offset $\Delta x(s)$ according to $\Delta x(s) = D(s) \cdot \frac{\Delta p}{p_0}$. The value of $D(s_{BPM})$ at the location s_{BPM} of a BPM can be determined by introducing a slight momentum offset (as described for the chromaticity measurement) and a position measurement. A plot of the position offset versus the momentum deviation delivers the dispersion at this location as discussed in Refs. [1, 3].

4 Measurement of beam profile

The transverse beam profile can be influenced by quadrupole magnets installed transfer lines. A measurement is important to control the beam width, as well as the transverse matching between different part of an accelerating facility. In a transport line, a large number of bending, focusing, and correction magnets give rise to the need for many profile measurement stations. Usually, the size of an electron beam is less than 1 mm, while proton beams have typically large diameters, up to some cm resulting in different technical requirements for the beam instrument. Depending on the beam particles, current, and energy, a large variety of devices exists; we can only briefly discuss the most popular ones. The beam spot can be directly observed by intercepting it with scintillator screens and viewing the emitted fluorescence with a camera. When charged particles with relativistic velocities pass a metallic foil, radiation is emitted as described by classical electrodynamics; the process is called optical transition radiation OTR. A camera records this light in an arrangement comparable to the one for scintillation screens. Secondary electron emission grids SEM-grid are widely used as an electronic alternative to achieve a large dynamic range; a grid of wires with typically 1 mm spacing is inserted. Instead of a fixed grid, one single wire can be scanned through the beam to get high spatial resolution; this is called Wire Scanner. A third approach is a so-called ionization profile monitor IPM, where the ionization products of the interaction of the beam with the residual gas atoms or molecules inside the non-perfect vacuum of the tube are detected. In these devices, the resulting electrons or ions are accelerated by an external electrical field to a detector having a spatial resolution. The ionization profile monitor is well suited as non-destructive methods for proton synchrotrons. High energetic electrons emit synchrotron radiation if the trajectory is curved. Monitoring this light by synchrotron radiation monitors SRM yields direct information about the beam spot.

4.1 Scintillation screen

The most direct way of beam observation is recording the light emitted from a scintillation screen intersecting the beam, monitored by a commercial video, CMOS (complementary metal-oxide-semiconductor) or CCD (charge-coupled device) camera as reviewed in Refs. [35–38]. These devices are installed in nearly all accelerators from the source up to the target and is schematically shown in Fig. 37 together with a realization where the pneumatic drive mounted on a Ø200 mm flange.

When a charged particle penetrates a material the energy loss (as discussed in Section 2.3) can be transformed to fluorescence light. In Table 4 some properties for frequently used scintillator materials are given; for more details see [15, 37, 39]. The important properties of such a scintillator are:

– High light output matched to the optical system of the camera in the optical wavelength range of 400 nm $< \lambda <$ 700 nm.
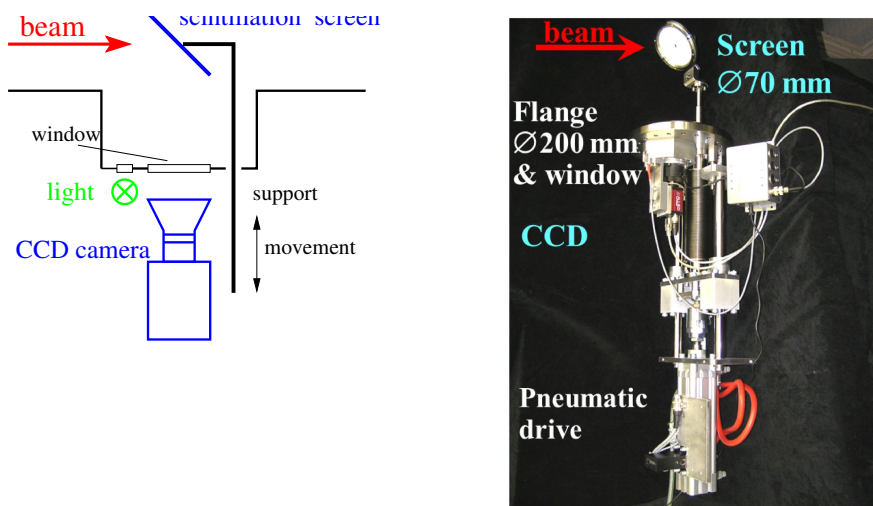
Fig. 37: Left: The scheme of a intercepting scintillation screen is shown. Right: A photo from a P43 phosphor scintillation screen of Ø70 mm and the CCD camera are mounted on a Ø200 mm flange with pneumatic drive is depicted.

Table 4: Chemical composition and some basic optical properties of inorganic scintillation screens. The last four materials are so called phosphor screens, where powder is deposited on glass or metal plates.

Abbreviation	Type	Material	Activator	max. emission	decay time
Quartz	glass	SiO_2	non	470 nm	< 10 ns
Alumina	ceramics	Al_2O_3	non	380 nm	∼ 10 ns
Chromox	ceramics	Al_2O_3	Cr	700 nm	∼ 10 ms
YAG	crystal	$Y_3Al_5O_{12}$	Ce	550 nm	200 ns
LuAG	crystal	$Lu_3Al_5O_{12}$	Ce	535 nm	70 ns
Cesium-Iodide	crystal	CsI	Tl	550 nm	1 μs
P11	powder	ZnS	Ag	450 nm	3 ms
P43	powder	Gd_2O_2S	Tb	545 nm	1 ms
P46	powder	$Y_3Al_5O_{12}$	Ce	530 nm	300 ns
P47	powder	$Y_2Si_5O_5$	Ce & Tb	400 nm	100 ns

– High dynamic range, i.e., good linearity between the incident particle flux and the light output. In particular, a possible saturation of the light gives rise to a deformation of the recorded profile.
– No absorption of the emitted light to prevent artificial broadening by the stray light inside the material.
– Fast decay time, to enable the observation of possible variations of the beam size.
– Good mechanical properties for producing up to Ø100 mm large screens.
– Radiation hardness to prevent permanent damage.

The material Chromox is a ceramic, which can be fabricated like pure Al_2O_3, used widely as an insulating material. The scintillation is due to the Cr activators; chemically it is comparable to ruby. The disadvantages are its long decay time of ∼10 ms and the large absorption inside the material. Nevertheless, due to its robustness, it is quite often used. The well-known Ce activated crystal materials like YAG ($Y_3Al_5O_{12}$:Ce) have better optical properties and are widely used for particle counting applications [15]. However, it is difficult to produce crystalline disks of about 10 cm diameter out of this material. Instead of the expensive single-crystal disk, one can use small grains of ∼ 10 μm sizes, deposited on several mm thick glass or metal disks. These phosphor screens are also used very fre-

707
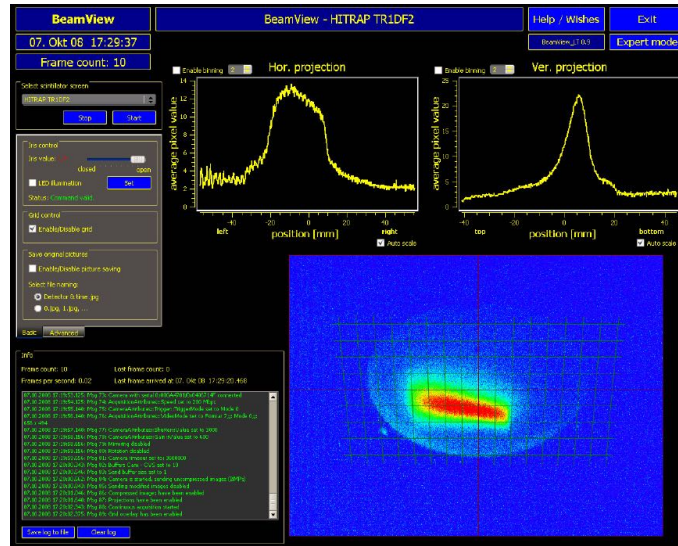
Fig. 38: Beam spot of a low current 4 MeV/u beam at GSI on a YAG:Ce screen recorded with a digital CCD camera. The original black-white image is converted to false-colour for better visibility. The projection on the horizontal and vertical axes are shown in the upper part [40].

quently in analogue oscilloscopes, electron microscopes and image intensifiers. P46 is an example for a phosphor screen powder offering a much lower production cost compared to the chemically equivalent single-crystal YAG:Ce. The properties of doped materials are strongly dependent on the activator concentration, therefore Table 4 gives only approximated values. The sensitivies of different materials span several orders of magnitude and depend on the particle species as well, see e.g. [36, 37]. As scintillation screens are used in all types of accelerators, a proper material choice is required. The beam image from a YAG:Ce screen is shown in Fig. 38 for a low current beam of only $\sim 10^6$ ions at 4 MeV/u, proving the high sensitivity of that material.

For high intensity beams, it must be ensured that the material is not destroyed by the absorbed beam power. In particular, for slow heavy ions with a range comparable to the screen thickness this restricts the use, see also the discussion in Section 2.3. A disadvantage of the screen is related to the interception. The used material is so thick (several mm) that it causes a significant energy loss, so it cannot be used for the diagnostics of a circulating beam inside a synchrotron.

4.2 Optical transition radiation screens

At electron accelerators with relativistic particles the profile is determined from the electromagnetic radiation at an intercepting thin metallic foil by the so-called **O**ptical **T**ransition **R**adiation **OTR**. Generally, light is generated by a classical electromagnetic process including special relativity, as caused by a charged particle passing from one medium into another. While passing to the vacuum in front of the foil, the particle has a certain electromagnetic field configuration, which is different from the field inside the medium, because the foil has a dielectric constant $\epsilon_r \neq 1$, i.e. different from the vacuum value. By approaching the foil, the particle's electromagnetic field leads to a time-dependent polarization at the foil boundary. When the charged particle transverses the foil, this field configuration is changed suddenly. The change of this polarization at the foil surface generates the radiation with a characteristic intensity and angular distribution.

A typical setup of an OTR measurement is shown in Fig. 39. The foil is inserted under an angle of 45° with respect to the beam path in most cases. The foil is made of Aluminum or Aluminum coated on Mylar with a thickness 1 μm or less. The light is emitted in the forward direction as well as at 90°,
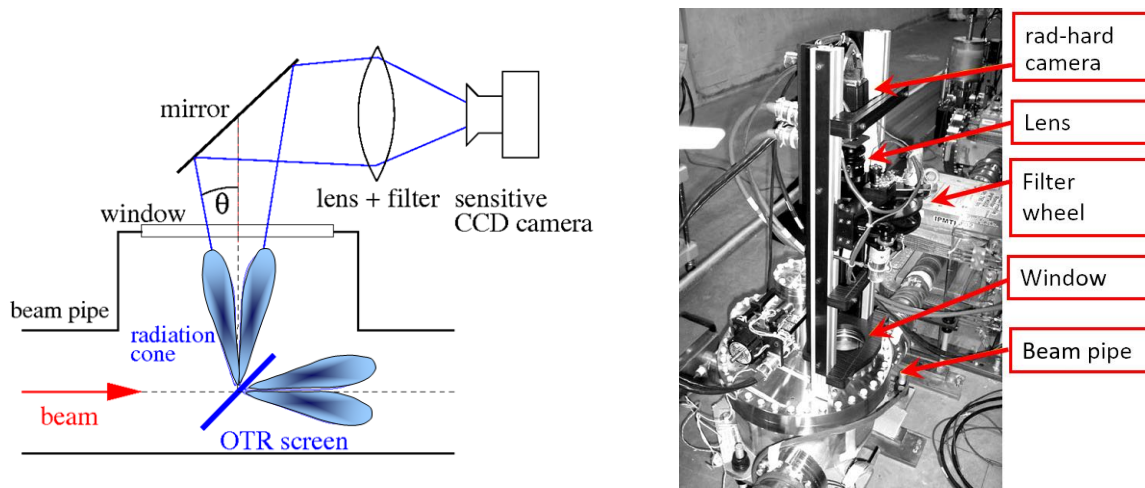
Fig. 39: Left: The scheme of an OTR screen measurement. Right: Photo for an OTR monitor at Fermilab [44]

because the metallic surface acts as a mirror. Depending on the particle energy, the angular distribution is peaked at the angle $\theta = 1/\gamma$ with γ the relativistic Lorentz factor. For typical values, 100 to 1000 beam particles yield one photon in the optical wavelength range. With appropriate optics, an image of the foil is recorded with a camera. For a technical perspective, the installation is comparable to the one of a scintillation screen but with a different intersecting target.

The general process is treated in e.g. [16, 41, 42] leading to closed but extensive formula. For relativistic beam particles and some other valid assumptions, the radiated energy $\mathrm{d}W$ emitted into a solid angle $\mathrm{d}\Omega$ per frequency interval $\mathrm{d}\omega$ can be approximated by

$$\frac{\mathrm{d}^2 W}{\mathrm{d}\Omega \mathrm{d}\omega} = \frac{2e^2\beta^2}{\pi c} \cdot \frac{\theta^2}{\left(\gamma^{-2} + \theta^2\right)^2} \tag{32}$$

with c, e, γ are the velocity of light, the elementary charge and the relativistic Lorentz-factor, respectively. The observation is oriented at an angle θ perpendicular to the beam path, the so-called specular angle, see Fig. 39. There is no difference concerning the radiation for electrons or protons moving with the same Lorentz-factor, reflecting the fact that only the electromagnetic fields of the beam particles are concerned. Note that the radiated energy does not depend on the frequency ω, i.e., the whole spectrum is covered. This is valid up to the plasma frequency of the metal, which is for most metals in the deep UV at about 10 eV. The radiated energy of Eq. 32 is converted to the number of photons by $W = N_{photon} \cdot \hbar\omega$ observed within a wavelength interval from λ_{begin} to λ_{end} in the optical region by the camera and integration over the interval $\lambda_{begin}...\lambda_{end}$. This yields the number of photons per solid angle

$$\frac{\mathrm{d}N_{photon}}{\mathrm{d}\Omega} = N_{beam} \cdot \frac{2e^2\beta^2}{\pi\hbar c} \cdot \log\left(\frac{\lambda_{begin}}{\lambda_{end}}\right) \cdot \frac{\theta^2}{\left(\gamma^{-2} + \theta^2\right)^2} \tag{33}$$

with N_{beam} is the number of beam particles. This function is plotted in Fig. 40 for three different values of γ. The radiation is more focused for higher energies, having the advantage that a larger fraction of the photon reaches the camera. At electron accelerators, OTR is used even at moderate energies above $\simeq 100$ MeV, corresponding to a Lorentz-factor $\gamma \simeq 197$. For protons this Lorentz-factor, or equivalent a beam energy for proton of 184 GeV, is only reached at some high energy facilities like at CERN SPS and LHC where OTR screens are installed [43, 44].

At modern, LINAC-based free electron laser facilities, the usage of OTR was hindered by te occurrence of so-called coherent OTR emission [45]. For intense, very short bunches (below typically 100 fs duration) with a longitudinal substructure (typically on the fs-scale), photons are emitted during a short
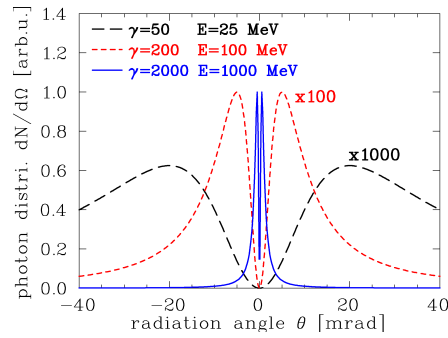
Fig. 40: The intensity distribution of OTR as a function of the observation angle for three different value of the Lorentz-factor γ. Additionally, the corresponding beam energies for electrons are given. The photon intensity is enhanced by a factor of 1000 for $\gamma = 50$ and 100 for $\gamma = 200$ in the plot.

time and from a small area. As these are electro-magnetic waves emitted with a phase and angular correlation, interference might occur leading to an interference pattern at the camera location. The detectable emission characteristic in terms of spatial distribution and wavelength spectrum depends significantly on longitudinal substructure of the bunch. For those beam parameters, the OTR-foil image does not represent the transverse beam distribution and exclude the usage of OTR for profile measurement; as an alternative scintillation screens were reverted at those facilities.

The OTR profile determination has some advantages and disadvantages compared to a scintillating screen measurement [46, 47]:

– OTR is mainly used for electron beams with energies above 100 MeV. For proton beams, the needed Lorentz-factor γ is only reached at the very high energy accelerators. Scintillation screens can be used for any beam and energy.
– The usable light emitted from an OTR screen depends significantly on the Lorentz-factor γ; for lower beam energies several orders of magnitude less light is emitted as compared to scintillation screens. Hence, more sensitive and expensive cameras have to be used for an OTR monitor.
– OTR is based on a classical electromagnetic process leading to linearity between the number of photons and the beam intensity (disregarding the aforementioned coherent photon emission for very short bunches). Scintillation is a more complex process and depends significantly on the material; saturation and radiation damage might occur, falsifying the profile reading.
– For the OTR process, the number of photons and their distribution is independent of the thickness of the foil. Hence, very thin foils of pure Al or Al-coated on Mylar foils down to 0.25 μm are used. Scintillation screens are generally thicker to guaranty their mechanical stability. For scintillation screens the amount of emitted photons scales with the thickness of the material. Hence, they are better suited for low intensity beams.
– OTR and scintillation screen are intercepting monitors. However, for OTR the thin foil minimizes the influence on the beam due to the low scattering probability. It can also be applied at high beam power, because of the low energy loss in the thin, low-Z material leading to a lower influence on the beam. Scintillation screens are thicker and the heating by the beam might modify the scintillation process. Moreover, most of the materials contain high-Z material leading to a larger energy loss.

15 wire spaced by 1.5 mm

15 ribbon spaced by 0.5 mm
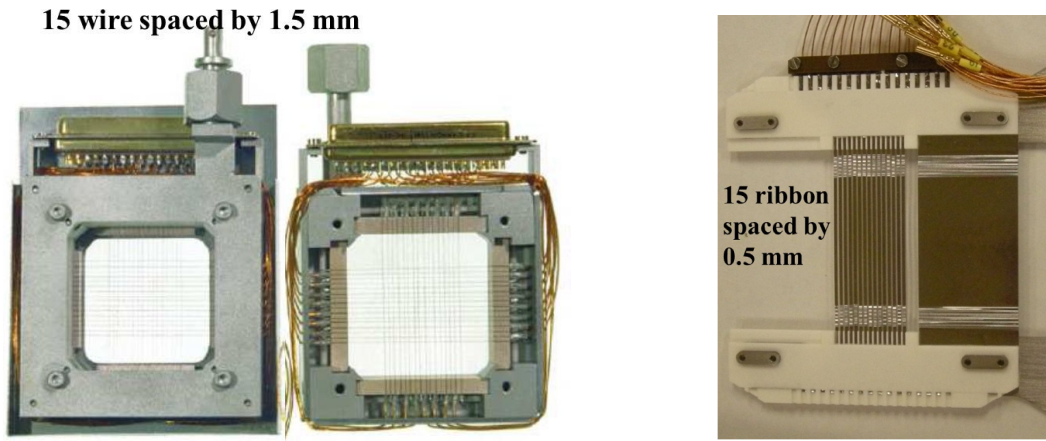
Fig. 41: Left: SEM-grid for both planes with 15 tungsten wires spaced by 1.5 mm as typically used at a proton LINAC. The individual wires are insulated with glass-ceramics.Middle: The same SEM-grid with removed tin cover. Right: SEM-grid based on ribbon made from 25 μm thick aluminium foil by laser cutting; the spacing is 0.5 mm. This type is used for high energetic proton above typically 1 GeV. The devices are mounted on a pneumatic drive to move it in and out of the beam (not shown).

4.3 Secondary electron emission grid SEM-grid

When particles hit a surface, secondary electrons are knocked-out form the surface, as described in Section 2.3.3. For the profile determination, individual wires or ribbons interact with the beam; this is called a **S**econdary **E**lectron **EM**ission **SEM-grid** or a harp as reviewed in [48]. Each of the wires has an individual current-to-voltage amplifier. This is an electronic alternative to a scintillation screen with a much higher dynamic range, i.e., the ratio of minimal to maximal detectable current is orders of magnitude larger. For the metallic wires of about 100 μm diameter and typically 1 mm spacing tungsten is often used owing their excellent refractory properties related to the very high melting temperature. In particular, at low energy LINACs this is important because no cooling can be applied due to the geometry. A photo of such a device is shown in Fig. 41 and the specifications are given in Table 5. For applications at higher beam energies, ribbons might be used as an alternative.

Table 5: Typical specification for a SEM-grid used at proton and heavy ion LINACs.

Parameter	Value
Diameter of the wires	0.05 to 0.5 mm
Spacing	0.5 to 2 mm
Length	50 to 100 mm
Material	W
Insulation of the frame	glass or Al_2O_3
number of wires	10 to 100
Max. power rating in vacuum	1 W/mm
Min. sensitivity of I/U-conv.	1 nA/V
Dynamic range of the electronics	$1:10^6$
Integration time	1 μs to 1 s

Generally, the SEM-Grid is mounted on a drive to be inserted into the beam path for the measurement. For low energies, at proton LINACs the particles are stopped in the material or undergo a significant energy loss. The ratio diameter-to-spacing of the wires determines the attenuation of the beam current (and of cause also the signal strength on the individual wires). Typically only 10 % of the beam area is covered by the wires, and in this sense, the profile measurement is nearly non-destructive. For
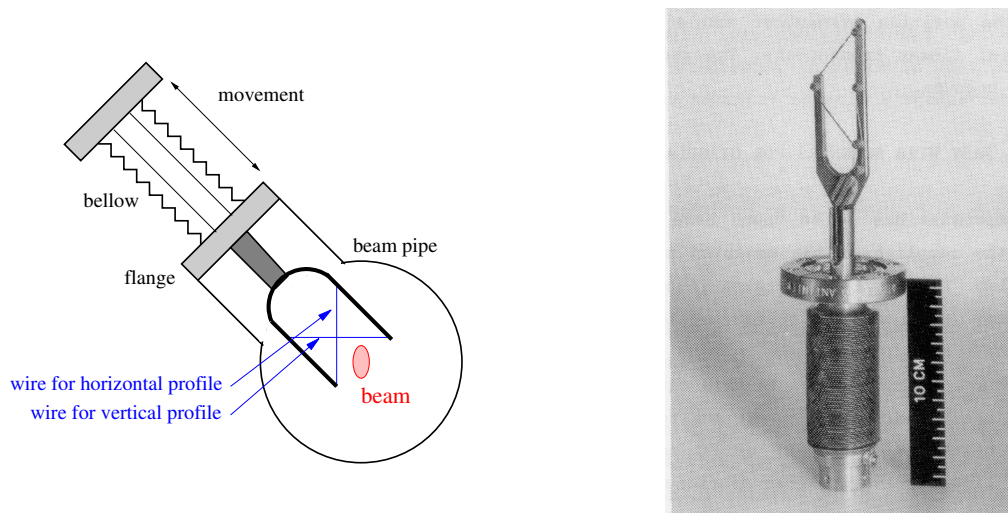
Fig. 42: Left: Schematics of the movement. Right: Linear scanner used at CERN [49]

energies above 1 GeV/u, the relative energy loss is negligible, and ribbons are used to increase the signal strength.
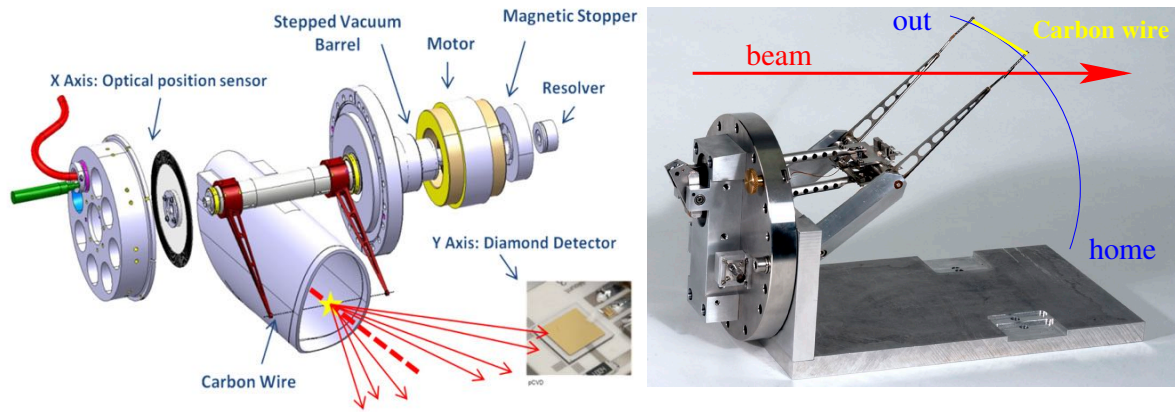
4.4 Wire scanner

Instead of using several wires with individual, expensive electronics, a single wire can be swept through the beam [48], which is called wire scanner. The advantage is that the resolution is not limited by the wire spacing and therefore this technique is often used at electron LINACs with beam sizes in the sub-mm range. It can also be applied in proton synchrotrons owing the small amount of intercepting matter.

There are two types of installations: We first discuss the *slow linear wire scanner*. The wire is mounted on a linear stepping motor drive for slow movement operated with a typical velocity of less than 1 cm/s with as depicted in Fig. 42. The slow wire scanner is used at many transfer lines at LINAC facilities for all types of beams. A resolution of 1 μm is reached in electron accelerators [50]. To get this low beam width reading σ_{beam} for a Gaussian beam, deconvolution of the contribution of the wire (4μm thick carbon wire in this case) from the measured width σ_{meas} has to be done according to $\sigma_{beam}^2 = \sigma_{meas}^2 - 4 \cdot r_{wire}^2$. In most cases, the wire is mounted on a fork, which is inserted into the beam pass by a drive mounted on 45°. Then only one drive is sufficient for measuring both transverse planes by mounting the wires in a crossed orientation, as shown in Fig. 42. If the signal generation is performed by reading the secondary emission current then two isolated wires can be mounted compactly on a type of fork. If the signal is generated by beam loss monitors outside the beam pipe, the two wires have to be separated (as shown in the Fig. 42 left), so the wires cross the beam one after the other.

An arrangement with a straight wire on a fast pendulum mechanics is a second type of so-called *fast flying wire scanner* often used at a proton synchrotron is depicted in Fig. 43 together with a schematic drawing of the entire arrangement. Scanning velocities up to 10 m/s can be achieved with a unique motor-driven mechanism. As the wire material, carbon or SiC is used due to its low weight and low nuclear charge Z, resulting in a low energy deposition in the wire (Bethe-Bloch Eq. 12 gives $dE/dx \propto \rho \cdot Z/A$). In addition, these materials can withstand high temperatures without melting. The thickness can be down to 10 μm. However, due to the single scanned wire, the profile is not taken at a single instant, even with high scanning velocity. Therefore only the steady-state distribution can be probed.

For the display of profiles, the position of the wire, determined by the position-encoder, is plotted on the horizontal axis. The beam signal for the vertical axis can be deduced from the current given by the emitted secondary electrons, like for a SEM-grid. This is done in particular for low energy protons and heavy ions. In most cases for beam energies larger than 150 MeV/u for ions (the threshold

712

Fig. 43: Left: Scheme of the entire detection system for a flying wire. Right: Pendulum scanner fork and wire used at CERN synchrotron [51].
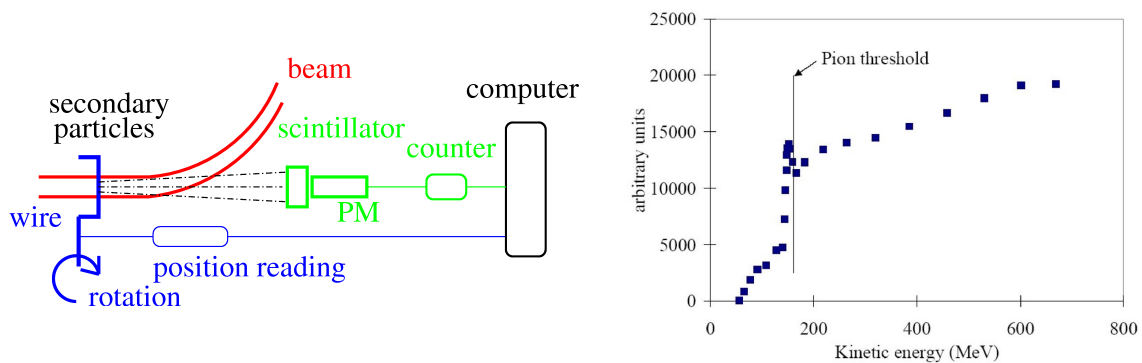

Fig. 44: Left: Scheme of a wire scanner using the production of secondary particles as the signal source. Right: The total rate from a wire scanner under proton impact at CERN PS-Booster, showing the rate increase above the π-threshold at ~ 150 MeV [52].

for π-meson production) or 10 MeV for electrons the signal is deduced by monitoring the secondary particles outside of the beam pipe, see Fig. 44. These secondary particles might be hadrons created by the nuclear interaction of the proton or ion projectiles and the wire, having enough kinetic energy to leave the vacuum chamber. For the case of electron accelerators, the secondary particles are mainly Bremsstrahlung-photons. The detector is just a beam loss monitor, e.g. a scintillator installed several meters away (see also Section 7). The count-rate is plotted as a function of the wire position as a precise representation of the beam profile.

The fast flying wire is mainly used for at synchrotrons where the fast scanning velocity of typically $v_{scan} = 10$ m/s results in only a few passages of the individual particle through the wire. For high energetic particles, the resulting energy loss is sufficiently small so that the particles can still be stored (more precisely: stay within the acceptance of the synchrotron). This enables the usage of flying wires as transverse profile diagnostics for the stored beam.

A comparison of the slow linear wire scanner and the SEM-grid shows advantages and disadvantages of both types [48]:

– With an SEM-grid the beam intensity is sampled concurrently, whereas a moving wire samples the parts of the profile at different locations at different times. Therefore variations of the beam intensity in time will be mixed with transverse intensity variations using a scanning device.

– In case of pulsed beams a synchronization between the readout of the electronics and the beam
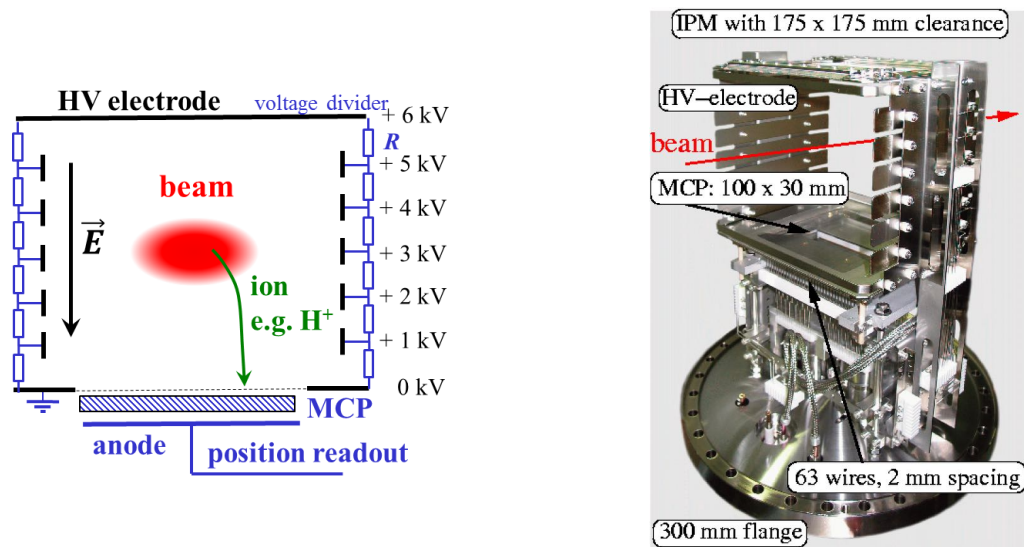
Fig. 45: Left: Scheme of an ionization profile monitor for the horizontal profile determination. Right: The large aperture ionization profile monitor installed at the GSI synchrotron for the horizontal direction. The readout behind the MCP (bottom) is done with an array of 63 wires with 2 mm spacing.

pulse is required as well as a movement within the beam pause. Synchronization between readout and beam pulse is easier to achieve for a SEM-grid.

– The resolution of a SEM-grid is fixed by the wire spacing (typically 1 mm), while a wire scanner can have much higher resolution, down to 10 μm, due to its constant movement.

– The electronics for data acquisition is cheaper for a scanning system. An SEM-grid requires one channel per wire.

– For the cost of the mechanics, it is vice versa: The precise vacuum actuator for the scanner is more expensive than the pneumatic drive needed for a SEM-grid.

4.5   Ionization profile monitor IPM

A frequently used non-destructive method for the profile determination is the **I**onization **P**rofile **M**onitor **IPM** sometimes also called **R**esidual **G**as **M**onitor **RGM**. These monitors are installed in nearly every proton synchrotron for the detection of beam sizes between some mm and several cm; a review is given in [53, 54]. The principle is based on the detection of ionized products from a collision of the beam particles with the residual gas atoms or molecules present in the vacuum pipe. A scheme for such a monitor is shown in Fig. 45. Due to electronic stopping process, electrons are liberated, and electron-ion pairs are generated. An estimation of the signal strength can be obtained by Bethe-Bloch formula Eq. (12) discussed in Section 2.3. Due to the single collision behaviour, the process can be approximated by considering some 100 eV for the creation of one electron-ion pair. To separate the electron-ion pairs, an external electric field of typically 1 kV/cm is applied by metallic plates installed in the vacuum pipe, but outside the beam path. To achieve higher field homogenity, guiding strips are installed at the side to get a smooth transition from the HV side to the ground plane. For most applications, the residual gas ions are detected in this setup. A realization from the GSI synchrotron is shown in Fig. 45 having a large opening of 17 cm [55]. For electron synchrotrons, IPMs are seldom used, due to the smaller electron beam dimensions.

Typical pressures for LINACs and transfer lines are in the range $10^{-8} - 10^{-6}$ mbar and for synchrotrons $10^{-11} - 10^{-9}$ mbar. For the LINAC case, the vacuum pressure is high, and the energy loss is larger due to the lower beam energy. Enough electron-ion pairs are generated to give a measurable current

714
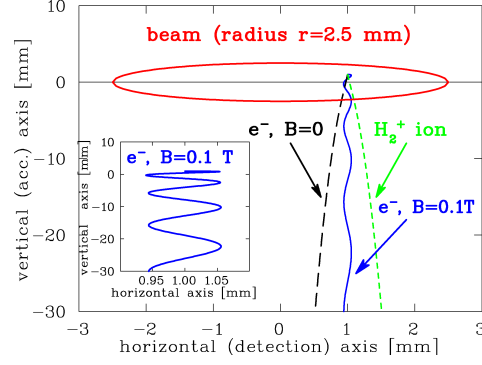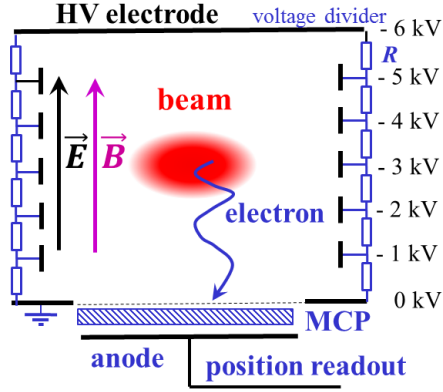
Fig. 46: Left: Schematic trajectory of an electron in an ionization profile monitor in the presence of a homogeneous electric E and magnetic field B. Right: The comparison of the trajectories of an H_2^+-ion and an electron with and without a magnetic field visualizes the broadening due to the beam space-charge field. By applying a magnetic field the electron is fixed to the field line, as shown in the insert. The beam parameters are: 10^9 U^{73+} within a 10 m long bunch with a radius of 2.5 mm.

(down to 0.1 nA per strip) of secondary ions for direct detection by a sensitive SEM-grid like wire array, e.g. [56]. In a synchrotron, the pressure and the stopping power is lower. A **M**ulti **C**hannel **P**late **MCP** particle detector acting as a 'pre-amplifier' to enable spatial resolved single particle detection [57, 58].

For the measurement of intense beams, detection of electrons is more suited to overcome the space-charge induced broadening as it causes a modification of the residual gas ion's trajectory, see Fig. 46. The HV is reversed, to accelerate now the negative electrons created by the beam interaction toward the detector. If an additional magnetic field B is applied parallel to the external electrical field, the electrons spiral around the magnetic field lines with the cyclotron radius $r_c = \sqrt{2m_e E_{kin,\perp}}/eB$ with $E_{kin,\perp}$ being the kinetic energy fraction perpendicular to the magnetic field. This transverse kinetic energy is determined by the initial transverse velocity given by the kinematics of the atomic collision. The cross-section depends on the beam and residual gas molecule properties [59], resulting in kinetic energies for the emitted electron up to keV for the typical case. The cyclotron radius, and therefore the detector resolution, is mainly determined by this initial energy and is nearly independent of the beam space-charge field. The projection of the trajectory in the plane perpendicular to the field is a circle with less than 0.1 mm radius (corresponding to the spatial resolution of the MCP) if a magnetic field of $B \simeq 0.1$ T is applied. The movement along the field is a linear acceleration with a typical time of flight of ~ 2 ns. The necessary magnetic field of about 0.1 T is generated in most cases with a dipole magnet.
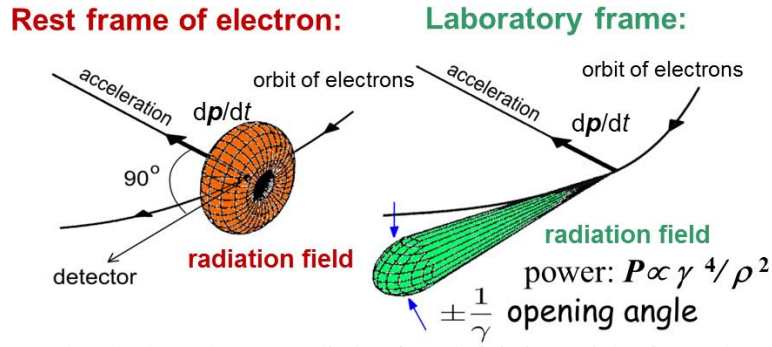
4.6 Synchrotron radiation monitor

For electron accelerators, the effect of synchrotron radiation, emitted by accelerated electrons, can be used for a profile determination. As known from classical electrodynamics [16] the radiation power P_{synch} for a momentum change dp/dt of a particle with mass m_0 is given by

$$P_{synch} = \frac{e^2 c}{6\pi\varepsilon_0 (m_0 c^2)^2}\left[\frac{dp}{dt}\right]^2 = \frac{e^2 c}{12\pi\varepsilon_0}\frac{\gamma^4}{\rho^2}. \tag{34}$$

For a circular accelerator, the direction of the momentum is changed in the bending dipole magnets of radius ρ leading to the emission of synchrotron radiation, which is significant only for relativistic energies with a Lorentz-factor above at least $\gamma > 100$. Therefore, the process is of relevance for typical electron synchrotrons (for electrons $\gamma = 100$ corresponds to $E_{kin} = 50.6$ MeV). However, for proton accelerators is can be only applied for energy above some 100 GeV (for protons $\gamma = 100$ corresponds to $E_{kin} = 92.9$ GeV).

Fig. 47: Forward peaked synchrotron radiation for relativistic particles from a bending magnet.
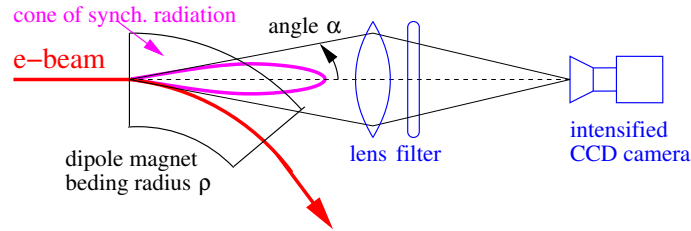
Fig. 48: Scheme for a synchrotron radiation profile monitor observing the radiation from a dipole.

In the centre-of-mass system, the radiation is emitted perpendicular to the momentum change. The Lorentz transformation to the laboratory frame gives a factor of γ, yielding a forward peak distribution with an opening cone of half-angle γ as demonstrated in Fig. 47.

The light emitted by the electron's bend in a dipole magnet can be used to monitor its horizontal and vertical beam profile, as schematically shown in Fig. 48 and reviewed in [60]. . For diagnostic purposes, the optical part of the emitted spectrum is observed in most cases by using optical band-pass filters. For this wavelength, high-quality optics are available, and standard CCD or CMOS cameras can be used. A typical resolution limit for the related optics is in the order of ~ 100 μm, as related to the diffraction pattern created at the finite size lenses and filters [60, 61]. A higher resolution can be achieved by observing the light from wigglers or undulators if they are installed in the synchrotron.

A realization of a synchrotron light profile monitor is shown in Fig. 49 at CERN LEP [62]. The bending radius is here 3.1 km and the diffraction gives the most significant contribution to the resolution by about $\sigma \sim 300$ μm, which is comparable to the real electron beam size close to the final energy. The setup consists of a metallic mirror to deflect the light out of the plane of the beam. Owing to the high power of the synchrotron radiation, the mirror has to be cooled, and possible deformations can spoil the optical quality. With the help of some curved mirrors, the light is focused, and an optical filter selects the wavelength range of blue or UV light and detected with a camera. Even though the resolution is not too high, this relatively straight forward system can be quite helpful due to its non-destructiveness, as demonstrated in Fig. 49 from the synchrotron light source APS [63].

An example for the application of a synchrotron radiation monitor is shown in Fig. 50 during the acceleration at the ALBA booster synchrotron [64]. For the two-dimensional beam image, the width in the horizontal σ_x and vertical σ_y direction can be calculated and compared to simulations. A decrease of beam size is visible due to adiabatic damping. However, there an additional contribution to the beam width by the relative momentum spread $\Delta p/p_0$ of the beam particles and the non-zero dispersion D at the measurement location as $sigma_{tot} = \sqrt{\varepsilon\beta + (D \cdot \Delta p/p_0)^2}$ and the contribution by the quantum fluctuations related to the emission of photons [64].

The diffraction limit of the standard monitor can be compensated by using an interference technique by a double-slit as known from astronomy. From the distance of the minima of the interference
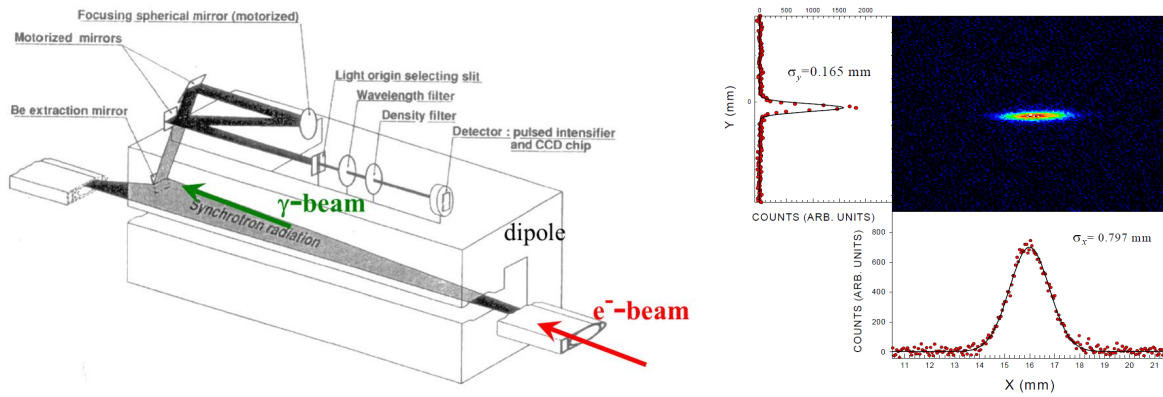
Fig. 49: Left: The synchrotron radiation profile monitor at LEP. The optical system is installed close to dipole magnet with bending radius of 3100 m [62]. Right: Image of the electron beam in the APS accumulator ring by a synchrotron radiation monitor [63].
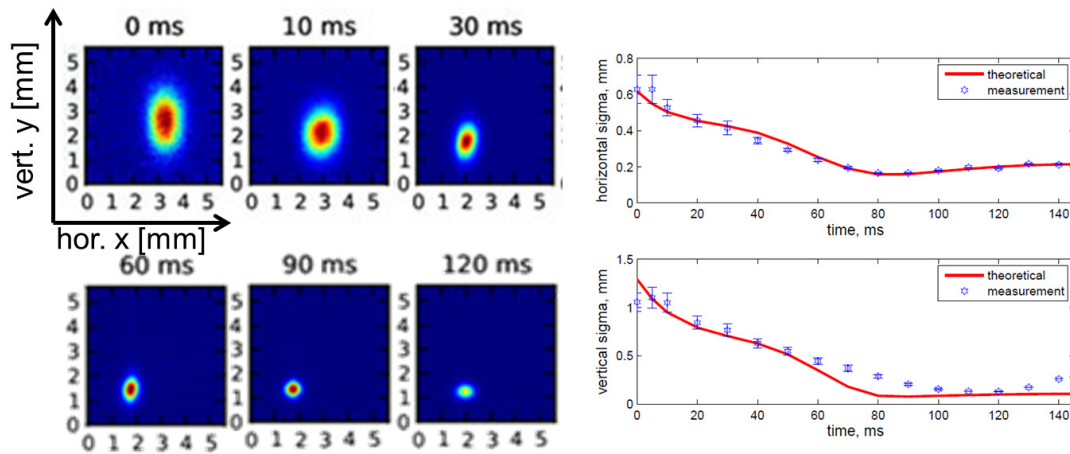
Fig. 50: Left: Examples of two dimensional beam image by a synchrotron light monitor at ALBA booster synchrotron. Right: The fitted horizontal and vertical beam width during the acceleration 0.1 to 3 GeV within 130 ms and the comparison to simulations [64].

pattern, the beam width can be calculated. Due to the non-coherent emission by an ensemble of electrons, the fringes fade-out for large beam sizes. A resolution down to the 1 μm range has been realized with this method in combination with an elaborated analysis tool, see e.g. [60, 65].

Another method to achieve a higher resolution is related to the observation of much shorter wavelengths. X-ray pin-hole cameras are used for this purpose. Only the emitted x-rays, scraped by a typically 20 μm aperture of high Z-material are recorded with a detector. An example is described in [66] A typical resolution concerning the beam width of 10 μm can be reached using such X-ray observation scheme [60]; but this requires a more sophisticated technical realization than for the observation in the optical range.

At dipoles in transfer lines, such synchrotron light monitors could be installed as well, which is realized at some facilities, e.g. [67]. However, there might be some technical problems as the amount of light emitted by the single pass of the electrons might be insufficient. Instead, OTR screens due to their more straightforward technical realization serve as a frequently used profile diagnostics in transfer lines.

5 Measurement of transverse emittance

The emittance describes the quality of a beam. Its determination is based on profile measurements; it is unimportant what method of profile measurement is used, as long as it has an adequate resolution. In the following, we start with a slit-grid device, where the spatial coordinate is fixed by an aperture and the angle distribution is measured. This is suited for particles having a range in matter below ~ 1 cm i.e. proton or ions with $E_{kin} < 100$ MeV/u. The emittance can also be determined by fitting the beam envelope, measured at one location with different focusing conditions or at different locations. This can be applied to transfer lines for all particle conditions. However, here it is problematic to include emittance growth due to space-charge forces, i.e., a blow-up of the transverse size due to the forces between the charged particles. A detailed review on the involved physics, technologies and data acquisition is given in [68].

In a synchrotron it is sufficient to measure the beam profile at one location only. For the stationary state of stable storage the orientation of the ellipse is fixed for a given location$s$. This is equivalent to the knowledge of the lattice functions dispersion $D(s)$ and β-function $\beta(s)$, is fixed. Therefore, only the absolute value ϵ is of interest. The emittance is calculated from the beam width σ via

$$\epsilon = \frac{1}{\beta(s)} \left[\sigma^2 - \left(D(s) \frac{\Delta p}{p} \right)^2 \right] \tag{35}$$

which is valid for the horizontal and vertical plane, respectively. If only horizontal bends occur in a facility, the dispersion in vertical direction is in most cases $D_y = 0$ and equation simplifies to $\epsilon_y = \frac{\sigma_y^2}{\beta_y(s)}$. Hence, the following discussion concerns transfer lines only.

5.1 Definition of the emittance

The motion of the beam particle can be described by a linear second-order differential equation. This assumes the absence of any non-linear coupling, like space charge forces or beam-beam effects as well as coupling between the two transverse and the longitudinal planes. The beam quality is given by the phase space volume, which is in this case a constant of the motion. The emittance for one plane is defined by

$$\epsilon_x = \frac{1}{\pi} \int_A \mathrm{d}x \mathrm{d}x', \tag{36}$$

where $A = \pi\epsilon$ is the area of the phase space occupied by the beam, see Fig. 51. A determination of the emittance is equivalent to the determination of the distribution of the spatial coordinate x (i.e. the beam profile), the distribution in angle x' and the correlation between x and x'.

The interpretation of an area assumes a hard-edge, homogeneous distribution. A more realistic case uses a density distribution $\rho(x, x')$ defined at the position of the vector $\vec{x} = (x, x')$ for each location s along the beam path. The profile distribution $P(x)$ is obtained by integrating the density ρ over x' as $P(x) = \int \rho(x, x') dx'$; the parameter $\sqrt{\sigma_{11}}$ is the standard deviation of this distribution. $\sqrt{\sigma_{22}}$ is the corresponding value for the angular distribution $P(x')$ obtained by integrating $\rho(x, x')$ over x as $P(x') = \int \rho(x, x') dx$. σ_{12} is called covariance as it describes the correlation between x and x' and is related to the orientation of the ellipse in the phase space. With the help of these three parameters σ_{ij} the so-called beam matrix $\boldsymbol{\sigma}$ can be defined in the following way:

$$\boldsymbol{\sigma}(s) = \begin{pmatrix} \sigma_{11}(s) & \sigma_{12}(s) \\ \sigma_{12}(s) & \sigma_{22}(s) \end{pmatrix} \tag{37}$$

at one location s in the beam line. The beam matrix $\boldsymbol{\sigma}$ is a representation of the beam ellipse at this location s and varies along the beam path. It is used in connection with the transfer matrix $\mathbf{R}$, which
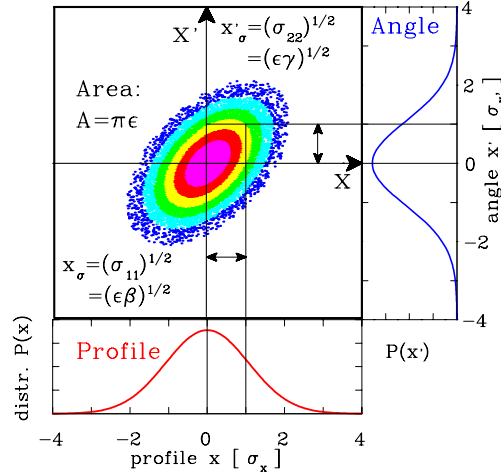
Fig. 51: The emittance ellipse and the projection to space- and angle coordinates for a Gaussian density distribution. The values of the independent variables are given in units of the standard deviation.

describes the action of the optical elements along the beam path in a linear approximation (i.e. for optical elements like drifts, dipoles, quadrupoles or solenoids) by

$$\boldsymbol{\sigma}(s_1) = \mathbf{R} \cdot \boldsymbol{\sigma}(s_0) \cdot \mathbf{R}^{\mathbf{T}} \tag{38}$$

from a location s_0 to s_1.

The absolute value of the emittance at each location can be defined using this notation as

$$\epsilon_x = \sqrt{\det \boldsymbol{\sigma}} = \sqrt{\sigma_{11}\sigma_{22} - \sigma_{12}^2} \tag{39}$$

and corresponds to an occupation of 15 % of the full phase space area. The unit of this value is m·rad or more frequently mm·mrad. To be consistent with the geometrical interpretation of an area surrounded by an ellipse, the number is multiplied by π; in this case 39 % of the beam is inside the area of $\pi \cdot \sqrt{\sigma_{11}\sigma_{22} - \sigma_{12}^2}$. In other words, the Gaussian beam quality at a given location s is fully described by the beam matrix $\boldsymbol{\sigma}(s)$.

Frequently the Twiss parameters are used, which are the beam matrix elements normalized by the emittance as

$$\alpha = -\sigma_{12}/\epsilon \qquad \beta = \sigma_{11}/\epsilon \qquad \gamma = \sigma_{22}/\epsilon. \tag{40}$$

The beam matrix is then

$$\boldsymbol{\sigma} = \epsilon \cdot \begin{pmatrix} \beta & -\alpha \\ -\alpha & \gamma \end{pmatrix} . \tag{41}$$

The width of profile- and angular distribution is given by

$$x_\sigma = \sqrt{\sigma_{11}} = \sqrt{\epsilon\beta} \quad \text{and} \quad x'_\sigma = \sqrt{\sigma_{22}} = \sqrt{\epsilon\gamma}. \tag{42}$$

Their geometric meaning is one standard deviation of the transverse profile and angular distribution of the beam. The geometrical size of the phase space ellipse is changed along the beam pass s; therefore the parameters $\alpha(s)$, $\beta(s)$ and $\gamma(s)$ are functions on the position s. In particular, for a synchrotron $\beta(s)$ is called the beta-function, describing the beam size via $x_\sigma(s) = \sqrt{\epsilon \cdot \beta(s)}$. For any arbitrary phase-space distribution the beam emittance can be calculated via the statistical moments of a 2-dimensional distribution $\rho(x, x')$.

To describe the beam quality via the emittance the *rms* value (*root mean square*) can be calculated as

$$\epsilon_{rms} = \sqrt{\det \begin{pmatrix} \langle x^2 \rangle & \langle xx' \rangle \\ \langle xx' \rangle & \langle x'^2 \rangle \end{pmatrix}} = \sqrt{\langle x^2 \rangle \langle x'^2 \rangle - \langle xx' \rangle^2} \tag{43}$$
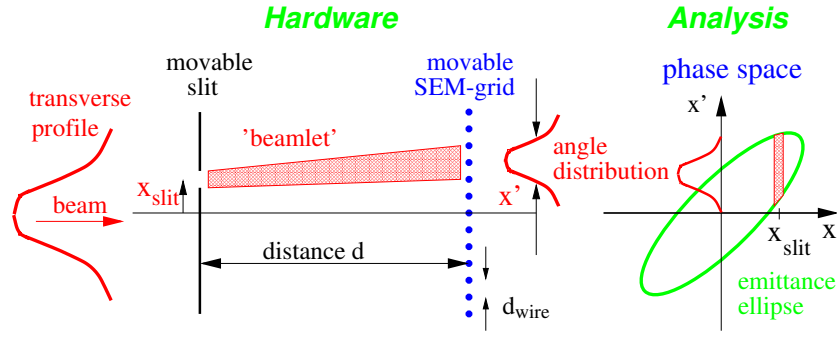
Fig. 52: Scheme of a slit-grid emittance measurement device.

using the statistical moments $\langle...\rangle$; this is equivalent to Eq. (39).

The emittance is a quantity defined in the laboratory frame due to the definition of the divergence. When a beam is accelerated, the divergence shrinks ('adiabatic damping') due to the changing ratio of longitudinal velocity v_s to transverse velocity v_x: $x' = v_x/v_s$. To compare emittance for different longitudinal momenta $p_s = m_0 \cdot \gamma_{rel} \cdot v_s$, the normalized emittance ϵ_{norm}

$$\epsilon_{norm} = \frac{v_s}{c}\gamma_{rel} \cdot \epsilon \tag{44}$$

is referred to a value $v_s/c \cdot \gamma_{rel} = 1$ with c is the velocity of light and $\gamma_{rel} = 1/\sqrt{1 - (v_s/c)^2}$ is the relativistic Lorentz factor. The normalized emittance is constant under ideal accelerating conditions.

A measurement of emittance means a determination of the numerical value of ϵ as well as the orientation and shape of the phase space distribution represented by the matrix elements σ_{ij} or the Twiss parameters α, β, γ correspondingly.

5.2 Slit-grid method

A popular method at proton or ion LINACs is the slit-grid device depicted in Fig 52, where the beam particles have a penetration depth below 1 cm. Here the position x is fixed for one direction with a thin slit having an opening of typically 0.1 to 0.5 mm to filter out only a small fraction of the beam at a known location. In the perpendicular direction, the full beam is transmitted to get a large signal. The angle x' is determined with an SEM-grid having a distance from the slit of 10 cm to 1 m depending on the ion velocity. In the field-free drift space the trajectories of the particles, combined in a 'beamlet', are straight lines. The angle distribution gives the contribution to the emittance plot in the phase space at the slit location. The slit is then scanned through the beam to get all positions. After making the full scan, the emittance is plotted, and the rms-value of the emittance ϵ_{rms} is calculated using the statistical moments as given in Eq. (43) from the measured data. A fit with an elliptical shape is drawn to the data, and the Twiss parameters can be calculated. An example is shown in Fig. 53 for a low energy ion beam as a contour or three-dimensional plot. This method can also determine more pathological phase-space distributions, not only Gaussian distributions. Close to an ion source, this happens quite often due to the large space-charge forces or the large profile width, where aberrations of the magnets could be significant.

According to Fig. 52, the resolution for the space coordinate Δx is limited by the slit width $\Delta x = d_{slit}$. The angle resolution $\Delta x'$, measured at the distance d, is given by the radius of the wire r_{wire} and the width of the slit resulting in $\Delta x' = (d_{wire} + 2r_{wire})/d$. The size of discrete elements in the phase space is given by $\Delta x \cdot \Delta x'$. This leads to a discretization error, in particular in the case of small beam sizes (focused beam) or small angle distributions (parallel beam). The resolution is improved by scanning the SEM-grid in steps lower than the distance of the wires d_{wire}, increasing the density of the discrete
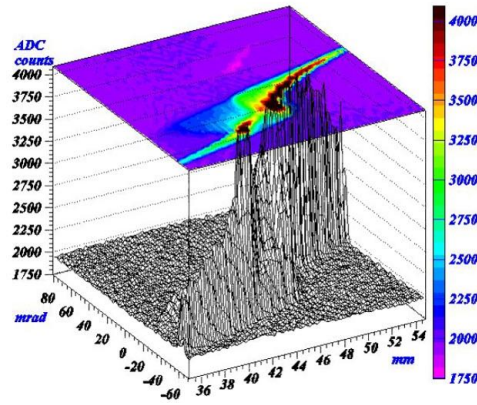
Fig. 53: Emittance measurement using a slit-grid device with a low energy Ar^{4+} ion of 60 keV at the Sprial2 facility depicting an mountain and contour plot [72].
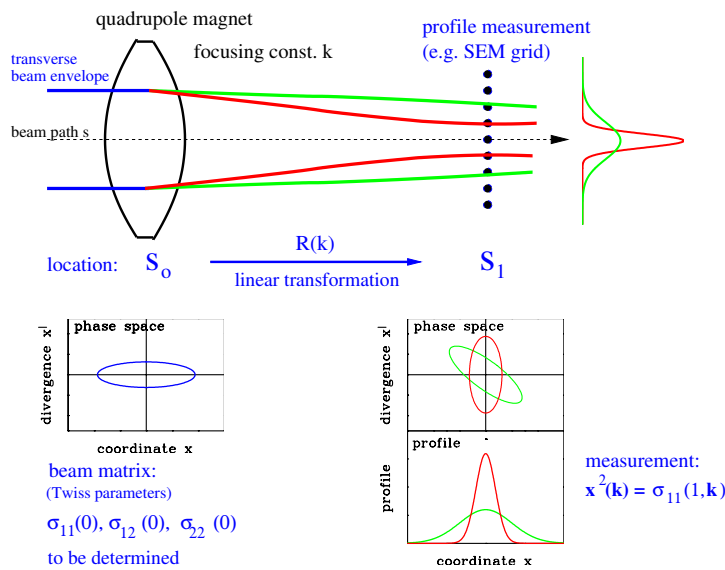
Fig. 54: Variation of a quadrupole strength for the determination of the emittance at the location s_0.

elements in the phase space analysis. This can lead to overlapping elements because their size $\Delta x \cdot \Delta x'$ stays constant. The same holds for a movement of the slit with a step size lower than the slit width.
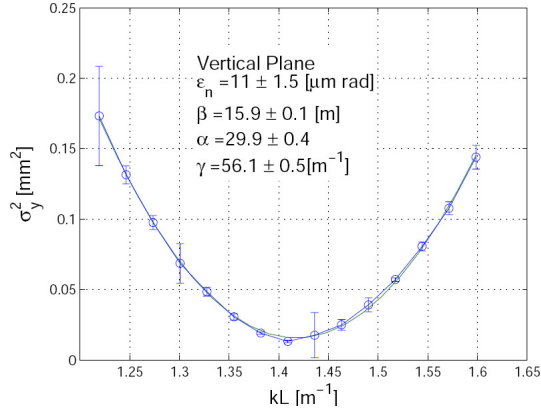
5.3 Quadrupole variation

At a transfer line, the emittance can be determined from a series of profile measurements by changing the focusing strength of a quadrupole as schematically shown in Fig. 54. To derive the emittance from such a measurement, linear transformations are used.

For a straight, non-dispersive transfer line, the transformation from a location s_0 to s_1 is given by the 2×2 transfer matrix $\mathbf{R}$. A determination of the emittance at the position s_0 is equivalent to the evaluation of the beam matrix $\boldsymbol{\sigma}$ at this position. The beam matrix is transformed to a second location s_1 with the help of the product of transfer matrices for the individual elements $\mathbf{R} = \prod \mathbf{R_{elements}}$ from the quadrupole to the profile measurement location via

$$\boldsymbol{\sigma}(1) = \mathbf{R} \cdot \boldsymbol{\sigma}(0) \cdot \mathbf{R^T} \tag{45}$$

721

Fig. 55: Profile width determined with a YAG:Ce screen at Elettra electron LINAC for a quadrupole variation and the parabolic fit [69].

The beam width $x_{rms}(1)$ is measured at s_1 and the equation for the element $\sigma_{11}(1)$ is given by

$$x_{rms}^2(1) \equiv \sigma_{11}(1) = R_{11}^2 \sigma_{11}(0) + 2R_{11}R_{12}\sigma_{12}(0) + R_{12}^2 \sigma_{22}(0). \tag{46}$$

This is a linear equation for the unknown three beam matrix elements $\sigma_{ij}(0)$ at location s_0, in Fig. 54 in front of the focusing quadrupole magnet. To get a solution, we need at least three different settings of the quadrupole strength k_i, and therefore different transfer matrices $\mathbf{R}(k_i)$ leading to three different readings of the profile width as depicted in Fig. 54. Assuming $i = 1, 2...n$ different settings of the quadrupole strength $k_1, k_2...k_n$ and n measurements of the beam width $x_{rms}^2(1, k_i) \equiv \sigma_{11}(1, k_i)$ a redundant system of linear equations is obtained in the form

$$
\begin{aligned}
\sigma_{11}(1, k_1) &= R_{11}^2(k_1) \cdot \sigma_{11}(0) + 2R_{11}(k_1)R_{12}(k_1) \cdot \sigma_{12}(0) + R_{12}^2(k_1) \cdot \sigma_{22}(0) \ \text{focusing } k_1 \\
\sigma_{11}(1, k_2) &= R_{11}^2(k_2) \cdot \sigma_{11}(0) + 2R_{11}(k_2)R_{12}(k_2) \cdot \sigma_{12}(0) + R_{12}^2(k_2) \cdot \sigma_{22}(0) \ \text{focusing } k_2 \\
&\vdots \\
\sigma_{11}(1, k_n) &= R_{11}^2(k_n) \cdot \sigma_{11}(0) + 2R_{11}(k_n)R_{12}(k_n) \cdot \sigma_{12}(0) + R_{12}^2(k_n) \cdot \sigma_{22}(0) \ \text{focusing } k_n
\end{aligned} \tag{47}
$$

The solution of this system are the values of the beam matrix $\sigma_{ij}(0)$ (or equivalently the Twiss parameters) at the location s_0, the entrance of the quadrupole magnet. With theses values, the size and orientation of the phase space ellipse is fixed. For three measurements (k_1, k_2, k_3) we can have a unique solution, but nothing is learned about the errors. Therefore, more than three measurements have to be performed, leading to a redundant system of linear equations. The solution is performed by a least-square fit to the best parameters of $\sigma_{ij}(0)$ or by solving the linear regression problem via so-called normal equations. Both algorithms are described in textbooks of Linear Algebra or Numerical Mathematics.

An example is shown in Fig. 55 performed at the electron LINAC at Elettra for a beam with 107 MeV using a YAG:Ce scintillation screen for profile determination. To get a small error for the emittance determination, it is recommended to pass a beam waist by the quadrupole variation. Only in this case, a parabola can be fitted through the profile data with sufficient accuracy.

Instead of solving the redundant system of linear equations depicted in Eq. (47), one can start from the parabola fit of the beam size squared as a function of the quadrupole strength as shown in Fig. 55. Most frequently the transfer line comprises of a quadrupole followed by a drift toward the profile measurement location. A quadratic dependence is observed for the following reason: Assuming a thin lens approximation with a focal length f of the quadrupole action one can write the transfer matrix as:

$$\mathbf{R_{focus}} = \begin{pmatrix} 1 & 0 \\ -1/f & 1 \end{pmatrix} \equiv \begin{pmatrix} 1 & 0 \\ K & 1 \end{pmatrix}. \tag{48}$$

722

After a drift of length L one gets the transfer matrix of the transfer line

$$\mathbf{R} = \mathbf{R_{drift}} \cdot \mathbf{R_{focus}} = \begin{pmatrix} 1 + LK & L \\ K & 1 \end{pmatrix}. \tag{49}$$

Inserting this matrix into Eq. (45) for the transformation of the beam matrix $\boldsymbol{\sigma}(1) = \mathbf{R} \cdot \boldsymbol{\sigma}(0) \cdot \mathbf{R}^T$ one gets for the measured beam matrix element $\sigma_{11}(1) = x_{rms}^2(1)$:

$$\sigma_{11}(1) = L^2 \sigma_{11}(0) \cdot K^2 + 2 \left(L \sigma_{11}(0) + L^2 \sigma_{12}(0) \right) \cdot K + \sigma_{11}(0) + 2 L \sigma_{12}(0) + L^2 \sigma_{22}(0) \quad . \tag{50}$$

This is the expected quadratic function in the quadrupole gradient K. From the beam width measurement for various quadrupole settings a parabola fit is performed as shown in Fig. 55. This yield the beam matrix elements σ_{ij} or the Twiss parameters α, β, γ as well as the albolute value of the beam emittance ϵ.

In the above discussion, it is assumed that the method is performed at a location where no dispersion D is present. The lattice function dispersion D gives rise to an additional contribution to the beam width Δx by the momentum deviation Δp of the particles with respect to the mean momentum p_0 as $\Delta x = D \cdot \Delta p / p_0$. The dispersion effect is added in a quadratic manner to the measured beam width as $x_{rms}^2 = \sigma_{11}(0) + (D \cdot \Delta p / p_0)^2$. To avoid the measurement of the lattice function D and the beam's longitudinal momentum spread, the location for emittance determination should be dispersion free. The described method is based on linear transformations and conservation of the emittance during the manipulation by the quadrupole. Moreover, an elliptical shape of the emittance is assumed. Depending on the general beam properties, this is a reasonable assumption as long as non-linear effects, like an aberration of magnets by higher-order field contributions or space-charge forces are low. If the investigations are done with intense beams, an emittance blow-up may occur, depending on the particle density, i.e., on the beam size. However, the size is to be changed, and even a waist has to be created. For high intensity beams, self-consistent, iterative algorithms have to be applied to get an estimation of the emittance at the quadrupole entrance, see, e.g. [70, 71].

6   Measurement of bunch structure

Longitudinal parameters are as important as the transverse ones. The longitudinal phase space is spanned by:

- The longitudinal spread of the bunch l is given in units of length (mm), time (ns) or phase (^{o} degrees with respect to the accelerating frequency), see Fig. 56. The mean value is the centre of the bunch relative to the rf or relative to the ideal reference particle. The corresponding transverse value is the transverse beam profile. For an un-bunched dc beam, e.g. in a proton storage ring, the quantity is of no meaning.
- The momentum spread $\delta = \Delta p / p_0$ is the deviation relative to the momentum p_0 of the ideal reference particle. Instead of the momentum, it is sometimes common for proton LINACs and cyclotrons to relate the quantity beam energy $\Delta E_{kin} / E_{kin}$ or even only ΔE_{kin} is given. The corresponding transverse value is the beam divergence distribution.

The value of emittance ϵ_{long} is given by the product of the two quantities

$$\epsilon_{long} = \frac{1}{\pi} \int_A \mathrm{d}l \mathrm{d}\delta. \tag{51}$$

where A is the area of the phase space occupied by the beam particles, see Fig. 56. Linear transformations can be applied in the same way as for the transverse case, see Section 5.1. The normalized longitudinal emittance

$$\epsilon_{long}^{norm} = \frac{v_s}{c} \gamma_{rel} \cdot \epsilon_{long} \tag{52}$$
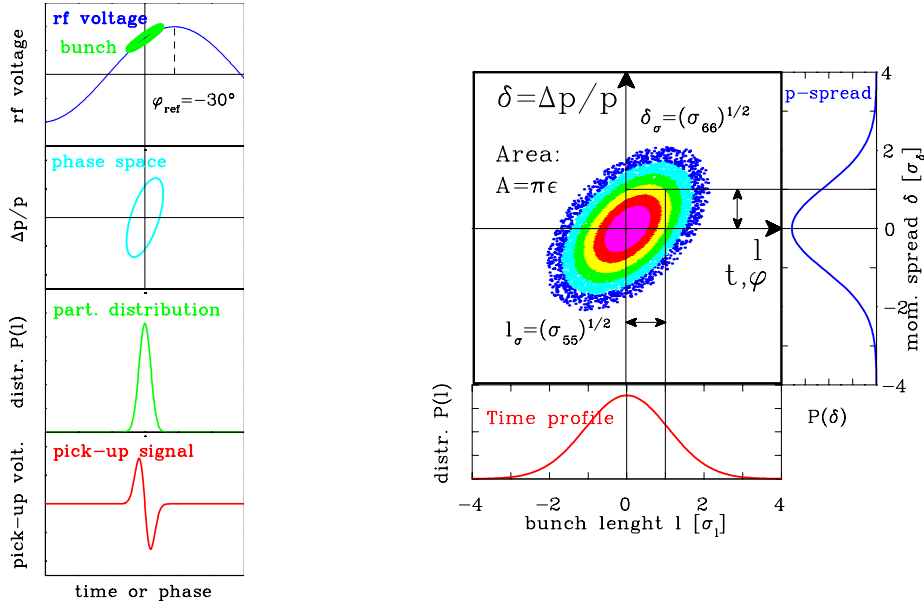
Fig. 56: Left: The relation between the accelerating voltage and the longitudinal emittance as well as the time distribution of the bunches as measured with the differentiated pick-up signal. Right: The longitudinal phase space plot of a Gaussian distribution.

is preserved under ideal conditions with v_s is the longitudinal velocity and γ_{rel} is the relativistic Lorentz factor.

Using a pick-up or a fast current transformer, the projection of the phase space on the time axis could be determined for some beam parameters, resulting in the bunch position and bunch structure. This is the case for most proton synchrotrons, and with the help of tomographic reconstruction, the full longitudinal phase space can be determined from a series of turn-by-turn bunch measurement, see, e.g. [12, 13]. However, some conditions have to be fulfilled for a pick-up or transformer to guarantee an adequate bunch shape measurement: Firstly, the signal from the pick-up or transformer must reflect the bunch shape, i.e. the frequency spectrum of the bunch must fit in the bandwidth of the recording electronics; for short bunches, e.g. at high energy electron accelerators this might not be the case, see Section 6.1. Secondly, the bunch has to be much longer in the longitudinal direction than the pick-up. For bunches with a length comparable to the pick-up, a further condition is that the beam must be sufficiently relativistic so that the beam's electric field is essentially transverse. For the transverse electric field component $\vec{E}_\perp$, Lorentz transformation [16] results an enhancement in the lab-frame compared to the rest-frame of the moving charge by

$$E_{\perp,lab}(t_{lab}) = \gamma_{rel} \cdot E_{\perp,rest}(t_{rest}) \tag{53}$$

tincluding the transformation of the time t_{rest} to t_{lab}. For bunches shorter than the pick-up, the signal does not reflect the longitudinal bunch shape. For electron beams, the bunch length is so short that the bunch structure is smeared out by integration on the pick-up capacitance; expressed in terms of electrical parameters by the limited bandwidth. Here the monitoring of synchrotron radiation is used in connection with the fast optical method using streak cameras. At LINAC-based light sources, the time resolution of a streak camera is insufficient and the method of electro-optical modulation is briefly discussed at the end of the section.

A measurement of the energy- or momentum spread $\delta = \Delta p / p$ is not discussed in detail here. A magnetic spectrometer can be used for this purpose, having a point-to-point focus in connection with small slits located at appropriate locations. This topic is described in textbooks on beam optics, e.g. in [73].
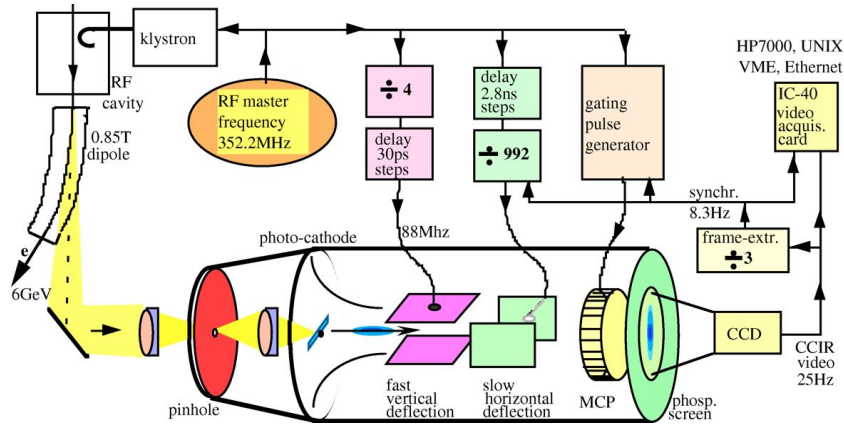
Fig. 57: Principle of a streak camera measurement for bunch width determination at electron accelerators ESRF [75].
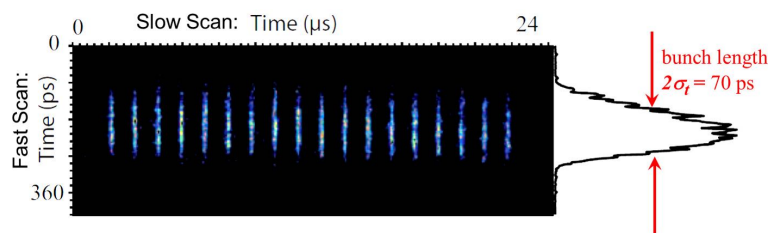

Fig. 58: Bunch length measurement with a streak camera, using synchrotron light from individual bunches emitted by the passage through a dipole at SOLEIL [76]. The horizontal axis scaling is 24 μs full scale for the bunch repetition (slow scan direction) and the vertical axis is 360 ps full scale for the bunch structure (fast scan direction).

6.1 Bunch structure measurement at circular light sources

In most cases, longitudinal diagnostics at electron accelerators is not done using pick-ups, although, due to the relativistic velocities, it would be possible. However, the bunch length, e.g. at a synchrotron light source is typically only of the order of several ten ps, so that even a pick-up bandwidth of several GHz is insufficient to reproduce the detailed bunch structure. Here we profit from the emission of synchrotron light at a dipole, or preferably from an insertion device. A review of this technique is given in [74].

The principle of such a measurement is shown in Fig. 57. It uses a streak camera as a commercially available device, which allows visible light observations with a time resolution down to typically 1 ps. The synchrotron light emitted by the bent electrons beam in the optical to UV wavelength range is used. It is focused and scraped by a pin-hole onto the photo-cathode of a streak camera. The photo-electrons from the photo-cathode are accelerated and pass a fast deflector driven by a frequency which is locked to the accelerating frequency for synchronization. After a certain drift space, the electrons are amplified by an MCP and converted to photons by a phosphor screen. With a standard camera, the phosphor screen image is stored. The different arrival time of the synchrotron light, and therefore the bunch structure, is converted to a difference in space with a full-scale of typically several 100 ps and a resolution in the ps range. A second, perpendicular pair of plates is driven with a much lower frequency to separate the images from the individual bunches.

An example of a bunch length measurement is depicted in Fig. 58 as performed with synchrotron radiation from a dipole [76]. The slow scan for the separation of the individual bunches is displayed in the horizontal axis. The vertical axis has a full scale of 360 ps and the bunch width is only $\sigma \simeq 40$ ps, demonstrating the high resolution of such a system. Those short bunches are needed by some synchrotron radiation users for time-resolved spectroscopy. Effects like head-tail oscillations or longitudinal bunch
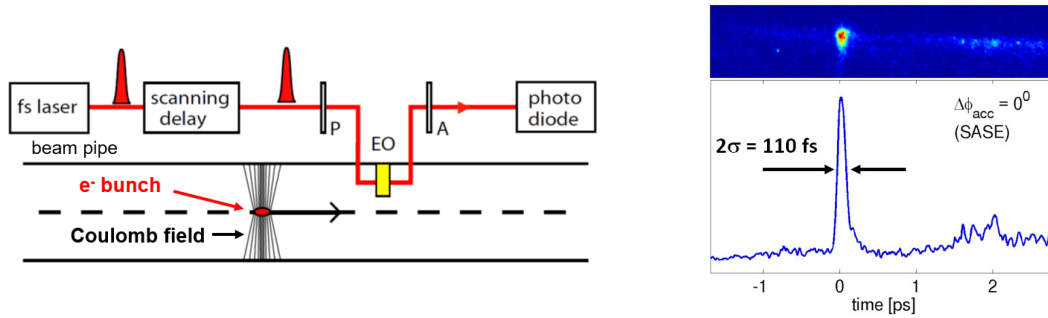
Fig. 59: Left: Electro-optical scanning by a short laser pulse for relativistic electron beams (P: polariser, A: analyser for the polarization, EO: electro-optical crystal), courtesy B. Steffen. Right: Single shot bunch structure measurement (camera image and projection) using EOTD at FLASH [79].

oscillation due to coupled bunch instabilities are visible with the help of the streak camera measurements as well, see, e.g. [74].

## 6.2 Electro-optical bunch structure measurement at linear light sources

At modern LINAC-based light sources, the process of free-electron lasing depends non-linearly on the temporal structure of the bunches. A typical bunch width is in the order of 100 fs with a non-Gaussian bunch structure and significant shot-to-shot variations might occur. The time resolution of ~ 1 ps concerning the light observation by the aforementioned streak camera is insufficient.

The technique of electro-optical sampling is suited for a time resolution down to some 10 fs. Electrons at that LINAC-based light sources are accelerated to highly relativistic velocities leading to an enlarged and temporally compressed transversal electric field as described by Eq. (53). This electrical field is detected by a birefringent crystal mounted typically 5 mm outside of the beam path, see Fig. 59 left. In most cases, a GaP or ZnTe crystal of thickness less than 100 μm is installed. The underlying effect of electro-optical modulation is a change of the index of refractivity between two orthogonal crystal planes depending on the external electric field; this leads to a rotation of the polarisation of transmitted light [77]. The rotation of polarisation, as caused by the time-dependent electric field of the electron bunch, can be probed by a co-propagating laser which is linear-polarised before the crystal. With the help of a subsequent analysing polariser, this is transferred to a time-dependent intensity modulation. A short laser pulse of typically 10 fs duration is used for the probing; at most installations a Titanium-Sapphire (Ti:Sa) laser or Ytterbium fibre laser crates the short pulse. In the basic installation, the arrival time between this laser pulse and the electron bunch is varied by an optical delay (i.e. varying path length of the laser light) to probe the temporal bunch structure as schematically depicted in Fig. 59. A photo of the beamline installation is presented in Fig. 60. This configuration is a scanning method (the controllable laser delay is varied each shot and acts as the time axis) and not suited in case of shot-to-shot variations of the electron bunches; therefore this method is seldom installed.

To enable a single shot observation, the setup is modified by two different methods as depicted in Fig. 61. The first method is called **E**lectro-**O**ptical **S**pectral **D**ecoding **EOSD**: Generally, a laser pulse of finite duration is composed by light within a range of wavelengths. An optical stretcher [77] separates the different wavelengths in time by a colour-dependent optical path length in a dispersive element like prisms, providing a correlation between the wavelength and the arrival time at the crystal. The electron bunch field temporally modifies the wavelength-dependent light in the electro-optical crystal. After passing the analysing polariser, the change in beam-induced polarisation is reflected in a wavelength-dependent intensity variation. By an optical spectrometer, this colour modulation is transferred to a spatial profile, which is finally monitored by a camera. The second method is called **E**lectro-**O**ptical **T**emporal **D**ecoding **EOTD** and is based on two laser beams: The same method of beam-induced

726
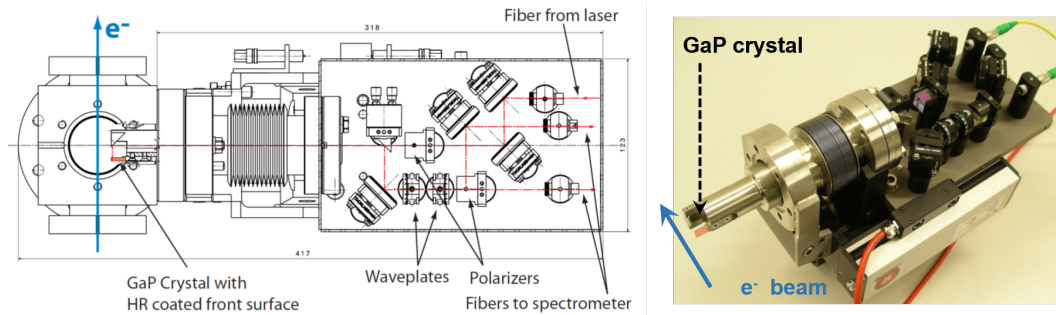
Fig. 60: Birefringent crystal and optics for an electro-optical bunch shape monitor at the PSI FEL [78].
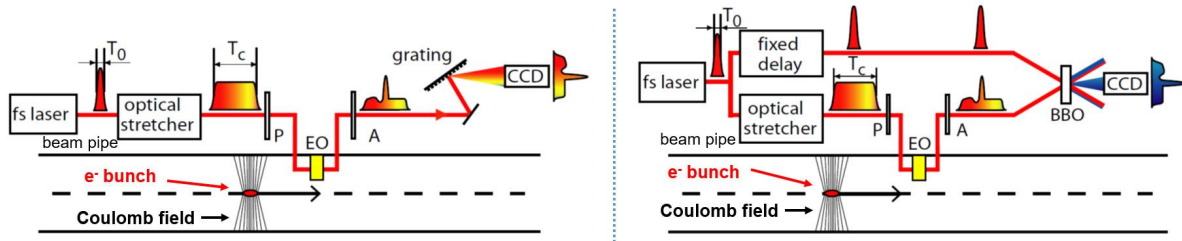
Fig. 61: Left: Scheme of the electro-optical spectral decoding EOSD method. Right: Scheme of the electro-optical temporal decoding EOTD method, courtesy B. Steffen.

modulation is installed. However, the original laser beam is spit before the optical stretching. Both laser beams are combined with an angle inside a non-linear crystal [77]. (Barium Boron Oxide BBO is often used for this purpose, providing a 2nd-harmonics generation as often used for frequency doubling of a laser beam.) The modulation detection is performed by frequency mixing of both laser beams as the non-linear crystal emitting the sum frequency of both laser beam, i.e. acts as a single-shot correlation measurement. Owing to the non-coaxial propagation inside the crystal, the light of the sum frequency is emitted from different locations, leading to a spatial separation of the beam-induced intensity modulation. Finally, a camera can monitor the related image. A detailed comparison of both methods is described in [79]. The achievable time resolution of the EOSD method is better than 50 fs. In contrast, the achievable time resolution by the EOTD method is about 25 fs. However, EOTD has the disadvantage of a larger laser power requirement related to the frequency mixing. A measurement of a single pulse of 100 fs duration at a FEL facility obtained by the EOTD method is shown in Fig. 59 right.

7   Beam loss detection

In a real accelerator, the transmission from the source to the target is never 100 %. The fraction of beam particles lost has to be controlled carefully to achieve optimal transmission. The lost beam particles cause some activation of the accelerator components by nuclear reactions. Moreover, the surrounding material can be destroyed by the radiation, as well as by the heating caused by the particles' energy loss. To detect the shower of secondary particle, as originated by nuclear interaction processes, a large variety of **B**eam **L**oss **M**onitors **BLM** exists. At nearly every high current accelerator facility, these monitors are installed for the protection of the accelerator components. The relatively cheap BLM instruments are mounted outside of the vacuum pipe at crucial locations as schematically depicted in Fig. 62. Their signals are a relevant information to prevent unwanted loss during the operation, e.g. caused by malfunctions of components. A careful analysis of the location and time structure of possible losses has to be performed before the choice of the suitable types of beam loss monitors can be made, see Refs. [1, 3, 80–82] for reviews.
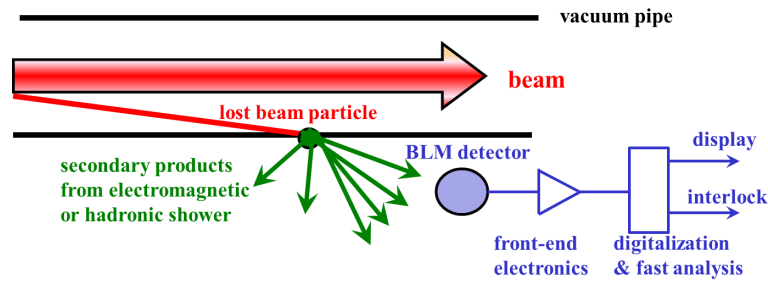
Fig. 62: Scheme for the installation of Beam loss monitors outside of the vacuum pipe.

7.1 Secondary particle production

When a high energy particle hits the vacuum pipe or any other material, secondary particles are generated. The relevant processes are described, e.g. in [83, 84]. Here only a brief overview is given:

– *Interaction of electrons:* For electron energies above $\sim$ 100 MeV, Bremsstrahlung dominates the slow-down process in materials, as shown in Fig. 11. The created high energetic γ photons give rise to further particles via $e^+ - e^-$ pair production. If the energy of the γ photons are high enough, other particles, like $\mu^\pm, \pi^\pm$... can also be produced, an electro-magnetic shower is generated. Moreover, the nucleus can be excited to so-called giant resonances: This is a collective nuclear excitation, where the neutrons oscillate against the protons. The dipole mode of these giant resonances has a threshold of about 6 MeV for typical materials. The de-excitation proceeds with high probability via neutron emission as a (γ, n) reaction. For higher energies also (γ, p) and (γ, np) channels are open.
When the electron is slowed down below $\sim$ 10 MeV, ionization loss by electronic stopping dominates, i.e. the creation of an electron vacancy at the atomic shell which is then filled by an outer electron leading to a soft x-ray emission. Those x-ray photons are absorbed within a short distance of mm to cm in typical metals.

– *Interaction of protons:* Beside electronic stopping, as shown in Fig. 10, nuclear interactions are possible. As a first step, we define the term 'thick target' for the case the interaction length is comparable to the range as given by the electronic stopping. In these thick targets, the probability of a nuclear reaction rises to nearly 100 % for energies above 1 GeV, see Fig. 63. Most of the final channels of these nuclear reactions include neutron emission. As an example, for the stopping of 1 GeV proton in copper or iron, $\sim$ 10 fast neutrons are liberated. The neutron yield scales approximately with E_{kin} for energies above 1 GeV. In addition, hadron showers (by the strong interaction) are possible, resulting in various species of 'elementary' particles.

Common to all interactions is the production of radioactive nuclei leading to activation of the accelerator components. The surrounding material relatively quickly stops the emitted charged particles. However, the neutrons, produced by most primary interactions, can travel long distances. Some of the beam loss monitors are therefore sensitive to these neutrons. Except for the production of radioactive nuclei, all processes are fast, compared to the timescale of interest in accelerator physics, i.e. faster than $\sim$ 10 ns. In this sense, a beam loss monitor reacts promptly to the particle loss. Owing to the kinematics of the primary interaction, the secondaries are emitted into a (more or less) forwardly peaked angular distribution. This leads to a spatial resolution of the loss detection by the monitor position close to the loss point.

7.2 Types of beam loss monitors

It is the task for beam loss monitors to localize the position and time of the loss. Their signals should be proportional to the amount of loss at this position. High sensitivity is needed to measure low losses.
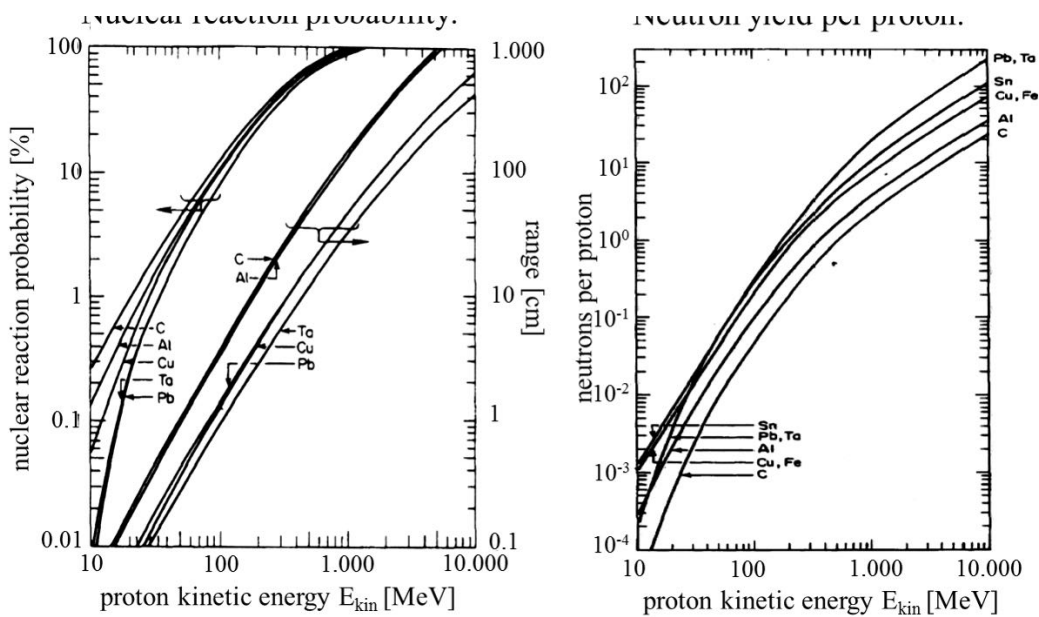
Fig. 63: Left: The ranges of protons in various metals and the probability of an inelastic nuclear reaction within the range as a function of the proton energy, i.e. within a thick target. Right: The total number of neutrons per proton incident on a thick target of various metals as a function of the proton energy [84].
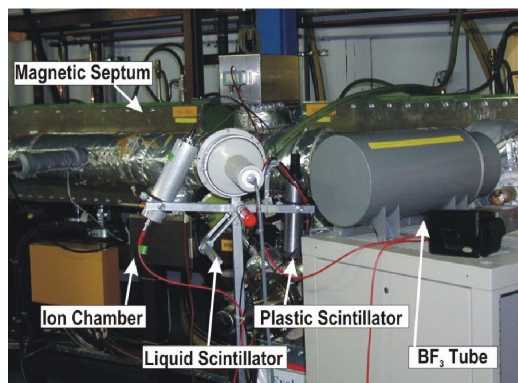

Fig. 64: The tested beam loss detectors installed at the extraction from the GSI heavy ion synchrotron [85].

A high dynamic range is required to deal with a sudden loss of a sizable fraction of the beam. Depending on the application, a bunch-to-bunch resolution on a ~ 10 ns time scale is needed, as well as up to 100 ms for a slow detection. All loss monitors are installed outside of the vacuum pipe, detecting mostly secondary particles. These can be neutrons, which are not much absorbed by the surrounding material, charged particles like protons, e^- and e^+ or γ-rays. Fig. 64 shows a photo of some frequently used types as tested at the GSI synchrotron. An overview of the different types is given in [1, 3, 80–82].

7.2.1 Plastic scintillators

Plastic scintillators detect charged particles owing to the electronic stopping, as discussed in Section 2.3. γ-rays are detected as they liberate electrons from the molecules via photo effect or Compton scattering; those electrons generate than the optical photons via their electronic stopping. Moreover, plastic scintillators are also sensitive to neutrons due to their elastic scattering on the hydrogen atoms of the polymers [15]. Due to the elastic scattering process generated by the relativistic neutrons, a large momentum transfer to the Hydrogen atoms of the macro-molecules is probable, which leads to a fast proton passing through the scintillator material and finally generates the light emission by its electronic stopping. The light is guided to a photomultiplier, converted to photo-electrons and amplified, see Fig. 65 (left)

729
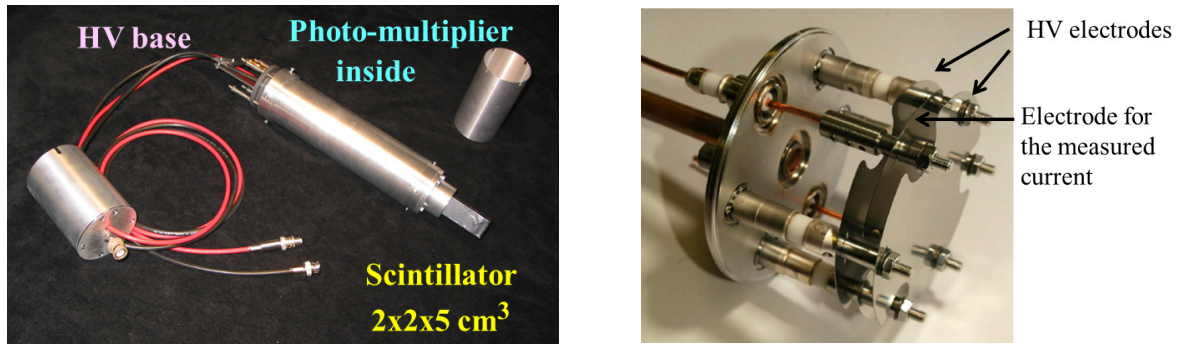
Fig. 65: Left: Photo of a typical BLM based on a plastic scintillator connected to a photo-multiplier. Right: Photo of a three plate SEM beam loss monitor [86].
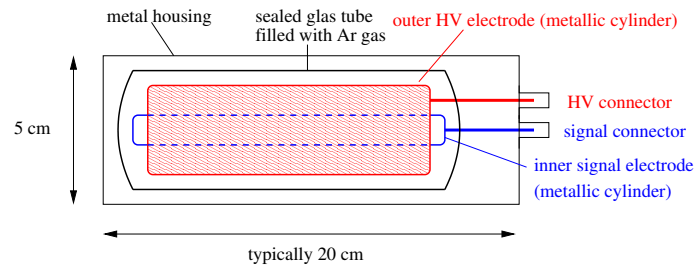
Fig. 66: Scheme of a co-axial ionization chamber as used for beam loss detection.

for a typical realization. In most cases the scintillation monitors are located in the crucial areas, like the injection or extraction devices, or close to scrapers. The disadvantage is the low radiation hardness of the plastic materials due to the complex chemical composition of the polymers from the plastic matrix.

7.2.2 Secondary Electron Monitor

In case the loss rate is very high, the current of secondary electrons from a surface is high enough to be measured directly. This can be realized for a secondary electron monitor by three plates installed in a small vacuum vessel [86]. The outer plates are biased by some +100 V and the secondary electron current emitted from the central plate is measured by a trans-impedance amplifier or a current-to-frequency converter. The inner part of such a monitor is shown in Fig. 65. Relevant simulations and tests of the response to different radiation are reported in [86].
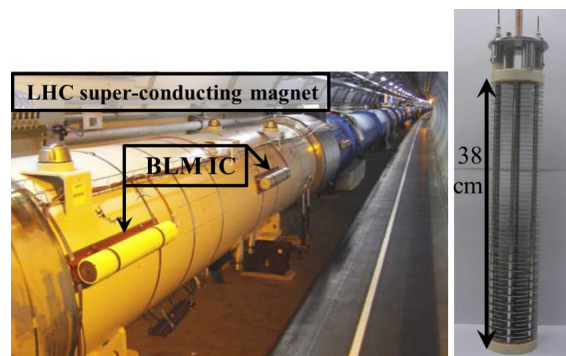
7.2.3 Ionization chamber

An Ionization Chamber **IC** [15] measure the number of secondary charges created in a gas volume. Fig. 66 shows such a round ionization chamber filled with Ar or N_2 gas. Typically, a sealed glass or metal tube contains $\sim$ 100...1000 cm^3 of gas between an outer high voltage electrode and an inner grounded and readout electrode [87]. The IC is not sensitive to neutrons and has a low detection efficiency for γ-rays, mainly charged hadrons and $e^\pm$ are detectable. By definition, the signal strength gives the absorbed dose directly in Gy. Because inert gases like Ar or N_2 are used in the detection volume, the device is very radiation hard. The signal strength is orders of magnitude lower than for detectors in a particle counting mode. In Fig. 66, the scheme of a co-axial IC is depicted. For this geometry, the IC does not react as fast as the scintillators, because the gas ions, created by the radiation, need $\sim$ 10 μs to reach the electrode. This time constant leads to a convolution of the primary signal, which for most applications is acceptable. The readout of the IC current by the digital electronics is therefore not faster than 1 ms in typical applications. The essential parameters for such an IC are summarized in Table 7.2.3. A typical installation of a co-axial IC at an accelerator beamline is depicted in Fig 67.

Table 6: Basic parameters for the so called RHIC-type co-axial IC [87] and the planar LHC-type IC [88].

Parameter	Co-axial IC	Planar IC
Outer length & diameter [cm]	20 & 6	50 & 9
Active gas volume [l]	0.11	1.5
Gas type & pressure [bar]	Ar at 1.1	N_2 at 1.1
Number of electrodes	2	61
Distance of electrodes [mm]	$\varnothing_{inner} = 6.3, \varnothing_{outer} = 38$	5.7
Voltage [kV]	1	1.5
Reaction time [μs]	$\simeq 3$	$\simeq 0.3$
Overall dynamic range	10^6	10^8
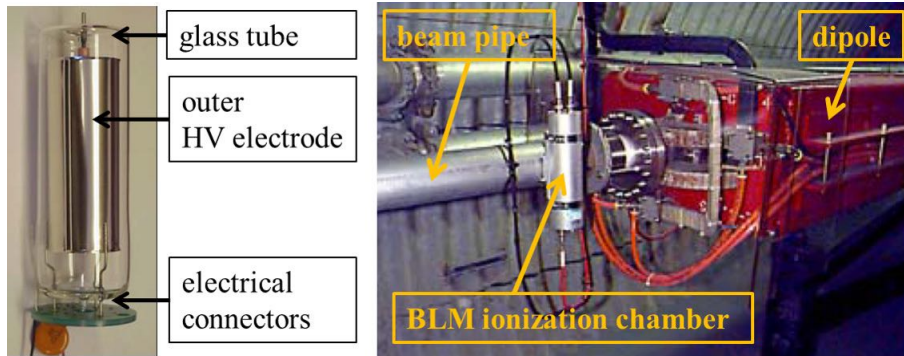
Fig. 67: Left: Photo of a 15 cm long co-axial ionization chamber used as a beam loss monitor. Right: The installation of such a ionization chamber for beam loss detection in a transport line.

Fig. 68: Photo of the installation of a 50 cm long ionization chamber comprising of 61 parallel plates at CERN LHC [88].

The detection threshold of an IC is proportional to the gas volume. To achieve a fast reaction time even for a large gas volume, the drift time of the gas ions and electrons should be shortened. This can be realized by a parallel electrode arrangement with alternating biased and readout electrodes. Such an IC is shown in Fig. 68 as installed at CERN LHC and other facilities. About 4000 BLMs are installed along the 27 km long LHC corresponding to an average distance of about 6 m. They serve as the main detectors for beam protection and can trigger a fast beam abortion. The design of such IC for LHC and relevant simulations concerning the response to various radiation species are discussed e.g. in [88].

The application of BLMs for beam operation and machine protection is discussed in the frame of the CAS lecture 'Machine and People Protection'.

8 Conclusion

The functionality of various beam instruments is described, and their applicability for different beam parameters are mentioned. For daily accelerator operation mainly current, position, and to some extent transverse profile measurements are executed. It is an advantage if the monitor is non-invasive for the beam, like current transformers and BPMs, to enable a simultaneous measurement at several locations, archiving of beam parameters, and, if possible for automated beam alignment by a feedback loop. Current transformers of various types serve as non-invasive instruments, but they have a lower detection threshold. For bunched beams, the transverse centre position can be recorded by BPMs. Due to their principle, BPMs are non-invasive but requires a minimum beam current to enable a sufficient precise position determination. The achievable position resolution is influenced significantly on the subsequent electronics: the spatial resolution can be balanced with respect to the observation duration (long time observation results in an improved position resolution). BPMs are the most frequently used monitors for beam alignment and serve in many cases as the sensor for a feedback loop. By exciting the beam to coherent oscillations, important synchrotron parameters, like tune and chromaticity, are determined with BPMs. For profile measurements, various techniques are applied, with scintillation or OTR screens being a favoured technique for regular operation for transfer lines due to their reproduction of the 2-dimensional distribution. SEM-Grids and wire scanners are also often used due to their robustness and large dynamic range. A non-invasive technique for profile measurements is realized by an IPM for medium to high intensity proton beams in transfer lines and synchrotrons. At electron synchrotrons, the anyhow available synchrotron light is used for transverse and longitudinal diagnostics. At transfer lines behind a LINAC or a cyclotron more complex parameter have to be determined, in particular the transverse and longitudinal emittances. The related measurements are, in many cases performed by experts during dedicated machine development times, which allow for more sophisticated instruments and methods. Bunch length measurement can be performed by recording the temporal structure of synchrotron light. However, at LINAC-based light sources at high time resolution is required, which is realized by electro-optical modulation techniques. A large quantity of beam loss monitors are installed to monitor the correct accelerator functionality permanently and generate an interlock in case of any malfunction to prevent for permanent activation or component destruction.

References

[1] H. Schmickler (Ed.), *Beam Instrumentation for Particle Accelerators, Proc. CERN Accelerator School 2018* Tuusula, CERN-ACC-2020-0010 (2020).

[2] V. Smaluk, *Particle Beam Diagnostics for Accelerators: Instruments and Methods,* VDM Verlag Dr. Müller, Saarbrücken 2009.

[3] D. Brandt (Ed.), *Beam Diagnostics for Accelerators, Proc. CERN Accelerator School 2007* Dourdan, CERN-2009-005 (2009).

[4] P. Strehl, *Beam Instrumentation and Diagnostics*, Springer-Verlag, Berlin 2006.

[5] M.G. Minty and F. Zimmermann, *Measurement and Control of Charged Particle Beams,* Springer-Verlag, Berlin 2003.

[6] S-I. Kurokawa, S.Y. Lee, E. Perevedentev, S. Turner (Eds.), *Proceeding of the School on Beam Measurement,* Proceeding Montreux, World Scientific Singapore (1999).

[7] P. Forck *JUAS Lecture Notes on Beam Instrumentation and Diagnostics*, available at the actual JUAS INDICO web-site and https://www.gsi.de/work/gesamtprojektleitung_fair/commons/ beam_instrumentation/research_and_development_rd/veroeffentlichungen.htm.

[8] Company Bergoz, www.bergoz.com.

[9] D. Belohrad, *Proc. DIPAC 11,* Hamburg, p. 564 (2011).

[10] R.C. Webber, *Proc. BIW 94,* Vancouver, p. 3 (1994).

[11] H. Reeg, *Proc. DIPAC 01,* Grenoble, p. 120 (2001).

[12] S. Hancock, M. Lindroos, S. Koscielniak, *Phys. Rev. Accel. Beams,* **3**, 124202 (2000) and CERN-PS-2000-068-OP (2000) and http://cern.ch/tomography.

[13] S. Hancock, J.L. Sanchez Alvarez,
CERN PS/RF Note 2001-010, http://cern.ch/tomography.

[14] W.R. Leo, *Techniques for Nuclear and Particle Physics Experiment,* Springer-Verlag Berlin (1994).

[15] G. F. Knoll, *Radiation Detection and Measurement*, John Wiley, New York (2010).

[16] J.D. Jackson, *Classical Electrodynamics*, John Wiley & Sons (1998).

[17] F. Ziegler, J.P. Biersack *SRIM*, see *The stopping and Ranges of Ions in Solids*, Pergamon Press (1985) and www.SRIM.org.

[18] M. Tanabashi et al., Phys. Rev. D **98**, 030001 (2018), Chapter 33, see also pdg.lbl.gov.

[19] O. Tarasov, D. Bazin et al., *LISE++* and subroutine *GOBAL*, lise.nscl.msu.edu/lise.html.

[20] A. F. D. Morgan, *Proc. DIPAC 05,* Lyon, p. 51 (2005).

[21] M.J. Berger et al. Code ESTAR, National Institute of Standards and Technology NIST, see http://physics.nist.gov/PhysRefData/Star/Text/ESTAR.html.

[22] C. G. Drexler, R.D. DuBois, Phys. Rev **A 53**, 1630 (1996).

[23] E.J. Sternglass, *Phys. Rev.* **108**, 1 (1957).

[24] R.E. Shafer, *Proc. BIW 89,* Upton, p. 26 (1989)
available e.g. at www.bergoz.com/en/mx-bpmf (1989).

[25] M. Wendt, *Proc. DIPAC 11,* Hamburg, p. 18 (2011).

[26] B.G. Pine, *CARE-ABI Workshop Lüneburg 2006,*
see adweb.desy.de/mdi/CARE/Lueneburg/ABI-Lueneburg.htm (2006).

[27] C. Boccard, *CARE-ABI Workshop Lüneburg 2006,* see
adweb.desy.de/mdi/CARE/Lueneburg/ABI-Lueneburg.htm (2006) and E. Calvo-Giraldo et al., *Proc. DIPAC 03*, Mainz, p. 187 (2003).

[28] A. A. Nosych et al., *Proc. IBIC 14,* Monterey, p. 298 (2014).

[29] R. Lorenz, *Proc. BIW 98,* Stanford AIP 451, p. 53 (1998).

[30] G. Vismara, *Proc. DIPAC 99,* Chester, p. 11 (1999).

[31] M. Wendt, *Proc. IBIC 14,* Monterey, p. 468 (2014).

[32] R. Jones, *Proc. BIW 10,* Santa Fe, p. 22 (2010), image: private communication.

[33] G. Rehm, *Proc. IBIC 19,* p. 479 (2019).

[34] R. Tomas et al., *Phys. Rev. Accel. Beams,* **20**, 054801 (2017).

[35] B. Walasek-Höhne, K. Höhne and R. Singh, *Video Cameras used in Beam Instrumentation - an Overview*, in H. Schmickler (Ed.), *Beam Instrumentation for Accelerators, Proc. CERN Accelerator School 2018* Tuusula, CERN-ACC-2020-0010 (2020).

[36] B. Walasek-Höhne et al., *Proc. IBIC 19,* Malmo, p. 242 (2019).

[37] B. Walasek-Höhne et al., *Proc. DIPAC 11,* Hamburg, p. 553 (2011) and workshop web-site http://www-bd.gsi.de/ssabd/index.html (2011).

[38] R. Ischebeck et al., *Phys. Rev. Accel. Beams* **18**, 082802 (2015).

[39] e.g. P. Lecoq et al., *Inorganic Scintillators for Detector Systems,* Springer Verlag (2006).

[40] R.Haseitl et al., *Proc. PCaPAC 2008*, Ljubljana, p. 180 (2008).

[41] Wartski et al., J. Appl. Phys. **46**, 3644 (1975).

[42] J. Bosser et al., Nucl. Instrum. Meth. **A 238**, 45 (1985).

[43] C. Bovet et al. *Proc. DIPAC 99,* Chester, p. 90 (1999).

[44] V.E. Scarpine et al., *Proc. PAC 07,* Albuquerque, p.2639 (2007).

[45] S. Wesch, B. Schmidt, *Proc. DIPAC 11,* Hamburg, p. 539 (2011).

[46] U. Iriso et al., *Proc. DIPAC 09,* Basel, p. 200 (2009).

[47] R. Jung, G. Ferioli, S. Hutchins *Proc. DIPAC 03,* Mainz, p. 28 (2003).

[48] M. Plum, *Proc. BIW 04*, Knoxville, p. 23 (2004).

[49] R.J. Colchester, R. Jung, *Proc. PAC 97,* Vancouver p.1917 (1985).

[50] C. Field, *Nucl. Instrum. Meth.,* A360, p. 467 (1995).

[51] S. Burger et al., *Proc. DIPAC 03*, Mainz, p. 122 (2003).

[52] U. Raich, *Proc. DIPAC 05,* Lyon, p. 1 (2005).

[53] P. Forck, *Proc. IPAC 10,* Kyoto, p.1261 (2010).

[54] P. Forck et al., *Proc. DIPAC 05,* Lyon, p. 221 (2005).

[55] T. Giacomini et al. *Proc. DIPAC 05,* Lyon, p. 150 (2005).

[56] J. Egberts et al., *Proc. DIPAC 11,* p. 547 (2011).

[57] T. Gys, *Nucl. Instrum. Meth.* **A 787**, 254 (2015).

[58] J.L. Wiza, *Nucl. Instrum. Meth.* **162**, 587 (1979).

[59] A. Allisy (Ed.), *Secondary Electron Spectra from charged Particle Interaction*, International Commission on Radiation Units and Measurement Report No. 55 (1996).

[60] G. Kube, *Proc. DIPAC 07*, Venice, p. 6 (2007).

[61] M. Wilke, *Proc. BIW 94,* Vancouver, p. 128 (1994).

[62] C. Bovet et al., *Proc. PAC 91,* San Francisco, p. 1160 (1991).

[63] B.X. Yang et al., *Proc. PAC 97,* Vancouver, p. 2215 (1997).

[64] M. Pont et al., *Proc. IPAC 11,* San Sebastian, p. 3023 (2011) and G. Benedetti et al., *Proc. IPAC 11,* San Sebastian, p. 2059 (2011).

[65] T. Mitsuhashi, *Proc. BIW 04,* Knoxville p. 3 (2004).

[66] M.-A. Tordeux et al., *Proc. DIPAC 2007*, Venice p. 180 (2007).

[67] B.K. Scheidt, *Proc. DIPAC 05,* Lyon, p. 24 (2005).

[68] J.M. Stockli, *Proc. BIW 06,* Batavia, p. 25 (2006).

[69] G. Penco et al., *Proc. EPAC 08,* Genoa, p. 1236 (2008).

[70] M.E. Schulze et al., *Proc. LINAC 00,* Monterey, p. 575 (2000).

[71] V.A. Dimov et al., *Proc. High Brightness Hadron Beam Conf. HB 16,* Malmö, p. 433 (2016) and references therein.

[72] P. Ausset et al., *Proc. DIPAC 09*, p. 110 (2009).

[73] H. Wollnik, *Optics of charged particles,* Academic Press (1987).

[74] K. Scheidt, *Proc. EPAC 00,* Vienna, p. 182 (2000).

[75] K. Scheidt, *Proc. EPAC 96,* Sitges, p. 1624 (1996).

[76] M. Labat et al., *Proc. DIPAC 07*, Venice, p. 241 (2007).

[77] See textbooks on optics, e.g. E. Hecht, *Optics*, Pearson Addison-Wesley (2016).

[78] B. Steffen et al., *Proc. DIPAC 09*, p. 263 (2009).

[79] B. Steffen et al., *Phys. Rev. Accel. Beams* **12**, 032802 (2009).

[80] K. Wittenburg, *Proc. EPAC 02,* Paris, p. 109 (2002).

[81] A. Zhukov, *Proc. BIW 10,* Santa Fe, p. 553 (2010).

[82] R.E. Shafer, *Proc. BIW 02,* Brookhaven AIP 648, p. 44 (2002).

[83] A.H. Sullivan, *A Guide to Radiation and Radioactivity Level near high Energy Particle Accelerators*, Nuclear Technology Publishing, Ashford (1992).

[84] S. Roesler, M. Silari, R.H. Thomas, *Radiation effects and protection,* in *A.W. Chao, K.H. Mess,*

M. Tigner F. Zimmermann (Eds.), Handbook of Acceleration Physics and Engeneering, World Scientific p. 767 (2013).

[85] P. Forck and T. Hoffmann, *Proc. DIPAC 01,* Grenoble, p. 129 (2001).

[86] D. Kramer et al., *Proc. DIPAC 07,* Venice, p. 313 (2007) and D. Kramer *Design and Implementation of a Detector for High Flux mixed Radiation Fiels,* PhD Thesis Technical University of Liberec (2008).

[87] R.E. Shafer et al., *Proc. Intern. Conf. High Energy Acc.*, Batavia, p. 609 (1983) and D. Gassner et al., *Proc. BIW 00*, Cambridge, p. 392 (2000).

[88] E.B. Holzer et al., *Proc. EPAC 08,* Genoa, p. 1134 (2008) and M. Stockner et al., *Proc. DIPAC 07,* Venice, p. 328 (2007).